THESIS

DEVELOPMENT OF A HIGH-VOLTAGE LASER TRIGGERED

SWITCH FACILITY INCLUDING INITIAL OPTICAL AND ELECTRICAL DIAGNOSTICS

Submitted by

Charles E. Rose

Department of Mechanical Engineering

In partial fulfilment of the requirements

For the Degree of Master of Science

Colorado State University

Fort Collins, Colorado

Fall 2019

Master's Committee:

    Advisor: Azer P. Yalin

    Carmen S. Menoni
    Mostafa Yourdkhani

SAND2019-12545 T

This paper describes objective technical results and analysis. Any subjective views or opinions that might be expressed in the paper do not necessarily represent the views of the U.S. Department of Energy or the United States Government

ABSTRACT

DEVELOPMENT OF A HIGH-VOLTAGE LASER TRIGGERED

SWITCH FACILITY INCLUDING INITIAL OPTICAL AND ELECTRICAL DIAGNOSTICS

Pulsed power programs have been part of the United States strategic plan to address the nation's energy and defense needs since the 1960s. With escalating energy demand, one of the greatest challenges of our time is to develop clean and reliable energy sources with controlled fusion being an exciting and favorable candidate. Developing this technology has been an arduous and taxing effort with a breakthrough (supposedly) coming just around the corner for decades. Arguably, one of the leading testbeds for fusion research is Sandia National Laboratories (SNL) Z machine which is part of SNL's pulsed power program. The Z machine can create fusion-like conditions and allows the global research community to investigate pathways forward to a viable fusion reactor. Integral to developing future pulsed power technology and the next Z-pinch style machines, high voltage spark gap switches are an active research area and the focus of this thesis.

Partnering with SNL this body of work details our efforts to develop a high voltage laser triggered switch facility at Colorado State University (CSU). We present the design and development of the Pulsed Power and Plasma Science Center (P3SC) along with preliminary diagnostic measurements of a millimeter gap length optically accessible high-voltage laser triggered switch (HV-LTS). The current thrust of the P3SC laboratory is to investigate switch closure plasma characteristics associated with recently discovered gaps in the Tom Martin switch model which describes temporal plasma channel resistance of these HV-LTSs. Basic background and theory of the Martin model are discussed including laying out two key assumptions we believe are related to the error recently found. Specifically, radial switch closure plasma channel growth

ii

fits an At^k trend (A and K are constants), and constant electrical conductivity are assumed both spatially and temporally. Considering extremely high voltages and nanosecond timescales of switch closure, direct measurements of these characteristics are extremely difficult. Therefore, we present contact and non-contact optical measurements that can be utilized to help inform the assumptions laid out herein. Specifically, a current viewing resistor (CVR) that was designed to withstand peak energies involved during switch closure was used to directly measure voltage, and subsequent current, associated with switch closure. CVR measurements along with triggering data allowed for determination of essential electrical characteristics common for HV-LTS technology. With knowledge of these macroscopic electrical characteristics a non-contact optical measurement scheme was devised to investigate switch closure plasma's more closely, including schlieren imaging and optical emission spectroscopy (OES). Specifically, temporal mapping of the switch closure plasma channel through direct imaging allows for characterization of radial growth (first assumption), and OES can be used to calculate electron temperatures which can be related to the electrical conductivity (second assumption). Given this backdrop we present key electrical characteristics on an optically accessible HV-LTS including: self-break behavior, switch run time, jitter, and equivalent circuit resistance and inductance. Further, radial plasma growth is measured (from intensified camera images) and found to agree with the Martin model assumptions, albeit with variability yielding a potential error in calculated resistance of ~15%. OES of switch closure plasmas are also recorded and show the spectra to be dominated by continuum at early times with emission lines becoming visible at ~200 ns after a 25 kV shot and ~500 ns after a 50 kV shot. This data, to the best of the author's knowledge, represents the first publication of HV-LTS emission spectra. With this data we have shown that the electrical conductivity assumption is the most likely cause of the error found in the Martin model. Continued investigation is warranted, and a more robust optical measurement like Thomson scattering is being considered to inform the Martin model and more generally the next generation of pulsed power technology

ACKNOWLEDGMENTS

No one achieves their goals alone….no one. Make time to thank those who help light the way

- February 2014, ME student at CSU, an impromptu guest lecturer Dr. Puttlitz describes a seminar that is offered to introduce students to faculty in the hopes of helping them transition to advanced degrees after graduation. I sign up for this seminar the next day

- June 2014, Put in notice to leave current job at restaurant to pursue work in mechanical engineering with no job prospects at this time

- November 30th, 2014 Meet my soon to be wife, Jenni, on my second to last day at the restaurant. I know right away that this is the one as she quietly explains she is a welder

- October 2014, Now in Dr. Puttlitz's seminar his friend Dr. Azer Yalin gives an impromptu lecture as original lecturer couldn't make it. I follow up and get a meeting with Dr. Yalin

- January 2015, Start working with Dr. Yalin at the Laser and Plasma Diagnostics Lab

- July 2016, Azer email's me and my colleague Ciprian Dumitrache to set up an experiment for Sean Simpson who works with Sandia National laboratory (SNL)

- September 2016, Ciprian and I travel down to SNL to help on an experiment and Sean asks if I would be interested in an Internship

- January 2017, Start designing P3SC lab

- June 2017, First round of Internships at SNL

- May 2018, Start to build P3SC lab with help from Jenni and her grandpa Al

- June 2018, Second round of internships at SNL

- September 2016, Finish building P3SC lab, Sean comes up to commission. Lab is up and running, start taking data for thesis

- July 2019, Data collection completed, and I am writing my thesis…this document, just after accepting a job offer from SNL. The course of my life has been changed forever

TABLE OF CONTENTS

LIST OF TABLES

LIST OF FIGURES

1. <u>Introduction</u>

1.1 What is Pulsed Power?

Pulsed power is a field of study that utilizes a low-power source to slowly charge up and store an immense amount of electrical energy, then discharge this stored energy rapidly as a compressed pulse; think lightning on command. Given that power is energy per unit time, as the pulse duration shortens the power increases dramatically. For example, if 1 Joule of energy is released over 1 second this would be 1 Watt, but if the same amount of energy was released over 50 ns would be 20 MW! The term "pulsed power" came after "pulse power" which was coined in 1964 by Physics International, a company that built pulse generators for these early pulse power systems[1]. In those days, a single stage of storage and discharge was common, and it wasn't until later that multiple stages of energy storage and discharge were synchronized together in a pulsed discharge configuration. An early adopter of this technology was the controlled fusion community which was using lasers as the primary driving mechanism for internal confinement fusion (ICF) experiments at this time[2].
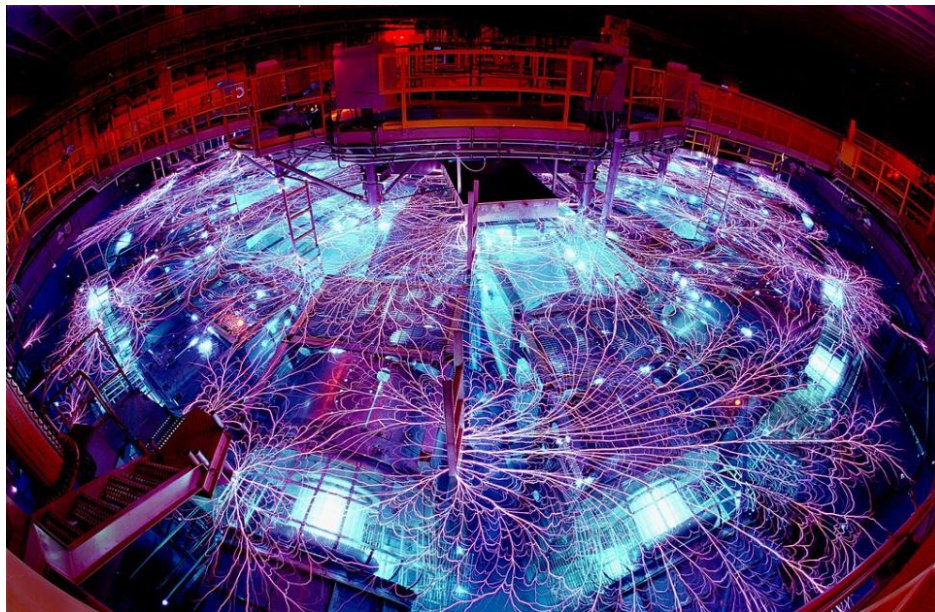
Figure 1-1: Sandia National Laboratories Z - machine. Credit: https://www.sandia.gov/z-machine

1

One basic approach to ICF is to deliver an enormous pulse of power to a tiny target forcing it to explode into a plasma then implode, heating the plasma to temperatures near those at the center of the sun[2,3]. Given this backdrop, the newly created pulsed power technology was an attractive candidate to deliver these intense bursts of power for ICF research. Following this time and through the 1970's, many pulsed power machines were built, but none larger than the one started in early 1977[2], the Electron Beam Fusion Facility1 (EBFA-1). This facility was the predecessor to what we know today as the Z machine (Figure 1-1). The Z machine is the world's most powerful laboratory radiation source and is capable of delivering millions of amperes to a target thereby driving plasmas to temperatures of over a million degrees Kelvin[2]. As the demand for a reliable and environmentally responsible energy source increases, pulsed power is poised to be one of the greatest tool's humans have ever created. Harnessing raw power similar to a lightning strike, but in the laboratory, it's also one of the most exciting fields of our time.

1.2 Research Motivation

Given the integral relationship between pulsed power technology and command fire high-voltage laser triggered switches (HV-LTSs), and that this technology is on the leading edge of controlled fusion research, there is a need for accurate predictive models of the behavior and characteristics of these switches. Historically, high voltage (HV) spark gap switches have been used for over 60 years[4-5] where extremely high voltages and currents are to be delivered. Electrical characteristics of these command fired switches are impressive and include extremely short and predictable delays with jitter on the order of ns to ps[6], along with the ability to carry kV-MV potentials at kA-MA currents[7,8]. Laser triggering of these HV switches has the potential to improve timing control and precision relative to other control schemes[7,9] particularly for multi-switch configurations. The basic approach is to use a pulsed laser source to generate optical breakdown in a region between the switch electrodes in the presence of the external electric field. The resulting laser-induced plasma facilitates switch closure and with the switch now fully "on",

current will flow and the plasma channel is maintained until the stored electrical energy is exhausted and the plasma decays. Switch designs can vary and include diverse variations of key components such as charging systems, energy storage and distribution methods, electrode shape, materials, etc. Further, variations exist in terms of triggering mechanisms including pulsed charging[10], field distortion[11], and laser triggering[4,7,8]. Considering this rich complexity, a great deal of literature has amassed on these switches[4-18,27-28,34] which continue to represent an active research area. One of the most important physical aspects of these HV switches is the electrical characteristics of the plasma channel that is formed when switching large potentials. To this end, one common model for HV switches came from T.H. Martin, in 1993[12], based on his work examining the energy losses that occur during switching. This model was developed to predict the time varying plasma resistance of the HV switches and has been used for research and development within the pulsed power community as a subroutine inside the transmission line code BERTHA[13]. While the Martin model has proven accurate for previous designs of HV-LTS's[14,15], recent iterations have uncovered gaps in the model's predictive nature[16]. This error typically manifests itself as under predicting switch rise time in a low inductance configuration due to an under prediction of the resistance drop during switch closure[16]. Martins' model has several key assumptions including: the main loss of energy is through radiation, thermal conductivity can
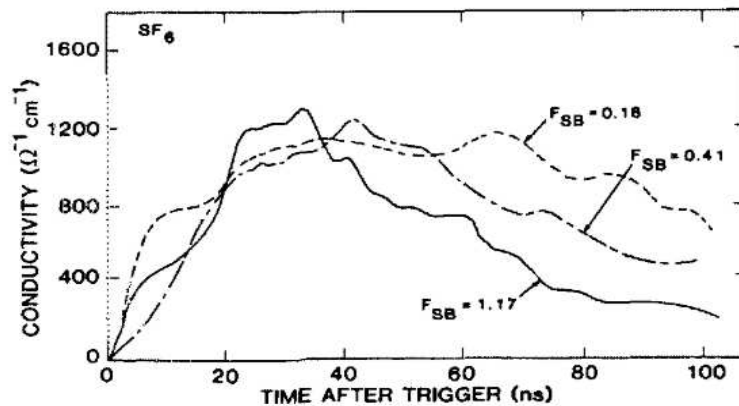
Figure 1-2: Electrical conductivity as a function of time delay from the initial laser trigger on a pulse charged HV-LTS: Credit Kushner et al.[17]

3

be neglected, radial plasma growth holds to an At^k trend, and the plasma electrical conductivity is constant temporally as well as spatially[12]. The first two assumptions are generally accepted by the community and the present research investigates the validity of the final two assumptions. With respect to the radial growth, limited HV-LTS data is available in the literature to test this assumption. Specifically, Martin gives two plots and Wolford et al.[17] provide a table containing radial growth collected via a streak camera.

With respect to the constant conductivity assumption, only one resource is known to us, by Kushner et al.[18] (Figure 1-2). This data (generated from electrical and radial plasma channel growth measurements) is in direct contradiction with Martin's constant conductivity assumption. Electrical conductivity can also be determined from electron temperature assuming the plasma is fully ionized[19] from the Spitzer conductivity[19,20]. For example, if the plasma is in local thermodynamic equilibrium (LTE), then electron temperature may be measured by optical emission spectroscopy (OES) using Boltzmann ratios[.21,22]. Data of this type is extremely limited, but Kushner et al.[18] estimated maximum electron temperatures of a pulsed charged water pulse forming line (PFL) HV-LTS between 2.7-4.7 eV. Given the lack of data in literature to examine these assumptions, this investigation aims at filling these gaps.

1.3 Basic HV-LTS Closure Theory

Focusing a sufficiently powerful laser pulse within the gap between the electrodes of a HV-LTS causes the generation of a laser induced plasma. For non-resonant breakdown, as we employ, initial seed electrons are formed through multiphoton ionization (MPI)[23,24,25]. These electrons are then accelerated and gain energy through inverse bremsstrahlung leading to electron avalanche[23,24,26]. When a laser plasma is formed between (or on one of) the electrodes of a HV-LTS, it serves as a highly conductive channel[27] which reduces the effective electrical distance between the electrodes. This increases the relative field stress and causes the remaining gap between electrodes to be bridged by streamer propagation[28]. Current begins to flow resulting

4

in Joule heating and widening of the channel[19]. Joule heating increases the temperature and conductivity, which allows yet more current to flow. With increasing current, the temperature and pressure increases sufficiently to develop a fully ionized plasma where the electrical conductivity can be related to the electron temperature through the Spitzer conductivity[18]. The plasma channel remains open for as long as the driving current persists. In the Martin model, based off of work by Braginskii[19], the expanding plasma front is treated as a "piston" traveling at supersonic speed driving a strong shock front at the interface of the plasma channel with the background gas. It is assumed that the shock-front temperature is much higher than the stationary background gas, and that the temperature in the channel is much greater than the shock itself. Therefore, by the time of current flow, the density of the gas in the channel must be very low as the major part of the mass of the moving gas is displaced from it. Given this outline and assumptions, the conservation equations of continuity, motion, and energy were solved, and a model of time-varying radial growth was put forward in 1958 by Braginskii[19]:

$$\frac{I^2}{\sigma} = 2\pi^2 \rho_0 \zeta (a\dot{a})^3 \tag{1}$$

where I is the current, σ is the electrical conductivity, ρ_0 is the initial gas density, ζ is a dimensionless constant (that varies somewhat between experiments) related to the radial growth (see below), a is the radius of the plasma channel and $\dot{a}$ is its first time derivative. The radial growth of the plasma channel is assumed to have the form:

$$a(t) = At^k \tag{2}$$

where A and k are constants associated with the channel growth, and t is time. Further, ζ is defined as:

$$\zeta = K_p \left(1 + \frac{2 - k^{-1}}{\gamma - 1} \right) \tag{3}$$

5

where K_p is the coefficient of resistance, assumed ~ 0.9 here[12,19], γ is the ratio of specific heats (c_P/c_v), and k is the constant derived from equation (2) by solving $\dot{a}/a$ for k:

$$k = \frac{\dot{a}t}{a} \tag{4}$$

Given this, equation (1) can then be re-written and integrated yielding:

$$\left(\frac{4}{\sigma\pi^2\rho_0\zeta}\right)^{\frac{1}{3}} \int I^{\frac{2}{3}}dt = a^2 \tag{5}$$

Ultimately, equation 5 is the final form that Martin uses to compute the plasma resistance, R, as:

$$R = \frac{L}{\sigma\pi a^2} \tag{6}$$

with L being the electrode gap length, and a^2 found from equation (5) based on the time-dependent current. Given ζ and σ were pulled out from the integral leading to equation (5), and all other terms are either constant or dealt with numerically (current), the observed error in the Martin model may be due to one or both parameters being time variant. Moreover, errors could also stem from the assumed form of the radial plasma growth found in equation (2).

1.4 Thesis Objectives and Outline

The main objectives of this body of work are as follows:

- Design and build a testbed enabling us to safely probe plasma characteristics of prototype HV-LTSs on nanosecond time scales
- Implement a suite of diagnostics including:
  - Electrical measurements (I.e. current viewing resistor, V-dot, B-dot)
  - Schlieren and direct imaging of laser generated switch closure plasmas
  - Optical Emission Spectroscopy (OES) of switch closure plasmas

- Use the testbed and diagnostics to investigate the major assumptions of the Tom Martin switch model given recently discovered gaps. This effort is in direct support of improving the design of next generation pulsed power devices.

The outline of this thesis is chronological with respect to the project, starting with design and development of the HV-LTS testbed in Chapter 2. Chapter 3 then describes the experimental procedures and techniques utilized to investigate the core assumptions to the Tom Martin switch model. Chapter 4 provides results and analysis including data on switch run time, jitter, 10-90 rise times, and initial switch closure plasma characteristics. Finally, Chapter 5 closes with our conclusions, describing our major findings and a path forward to future work.

2. <u>Design and Development of P3SC HV-LTS Laboratory</u>

2.1 Safety Concerns

The design of the Pulsed Power and Plasma Science Center (P3SC) HV-LTS Laboratory had a high emphasis on student and operator safety. High voltage on the order of 200 kV is necessary to meet the design specifications for some HV-LTSs. Further, the electrical energy stored, either in a capacitor, or some other medium can be several hundred to several thousand Joules, more than enough to deliver a lethal blow. This type of switch is command fired by an external pulsed laser, with pulse widths typically in the range of 5-10 ns reaching peak optical powers on the order of gigawatts. Laser powers on this order are more than enough to permanently blind or severely burn if struck on exposed skin. High pressure gas is required to fill the gap between electrodes at pressures ranging up to over a hundred atmospheres. Finally, a dielectric medium is necessary to cover all exposed high voltage components, typically oil or gas, and must be safely contained. Given this (non-exhaustive) list, the danger of this type of work should not be understated and having a safe lab space to carry out experiments is paramount. The lab design detailed below was created with these safety concerns in mind. Further, appropriate high voltage, capacitor, pressure, laser, and electrical safety training is required for all operators.

2.2 P3SC Facility and Infrastructure

Lab space used for this research is within the Powerhouse Energy Campus at CSU and has two access doors on the west face of the building (Figure 2-1). Both doors are capable of being locked from the outside, securing the experiment, while maintaining two egress points within the lab. The north-facing door is maintained locked, but still allows egress if necessary, while the east-facing door is used as the primary point of ingress and egress. A magnetically actuated switch on the main door acts as the
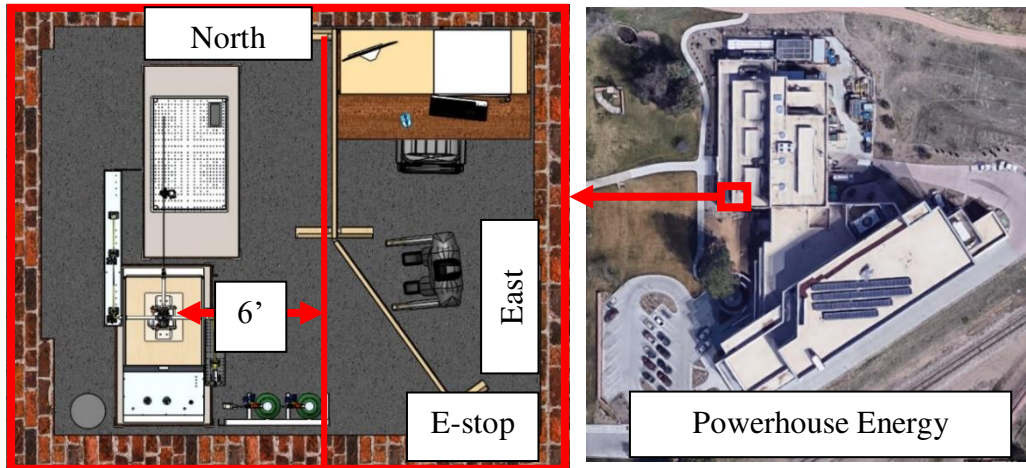
Figure 2-1: Left: CAD model showing top-down view of lab design. Right: Aerial top-down view of the Powerhouse Energy Campus at CSU showing lab location (credit – Google maps).

primary interlock signal. Equipment in the lab that is interlocked includes both HV DC power supplies, 125 VAC control relays, and the pulsed Nd:YAG laser used to trigger the HV-LTS. Both the power supplies and laser have latching type interlocks such that if the main door is opened this equipment will disable until re-enabled by the user (i.e., the equipment will not automatically re-energize upon door closure). An emergency E-stop was placed near the main door in the event the experiment needs to be rapidly shut down, either by the operator or an outside person entering the lab. Depression of the E-stop inhibits the sole wall outlet that powers the high voltage, pressure and laser equipment in the event the experiment must be abruptly aborted.

Several pieces of equipment were required to be designed and built including: a high voltage switch-tank housing the relays and HV-LTS, pressure system to safely deliver fill gas to the switch including bottle storage, a physical barrier to separate the experiment from the operator, and a master-slave control system to remotely operate the experiment (discussed below). Complete 3D design of the P3SC lab space was accomplished using SolidWorks before production began for ease of fabrication which was completely done in house. The high voltage switch tank required several iterations to achieve a suitable design meeting experimental constraints including: housing the HV-LTS and HV-relays, allowing for the trigger laser to enter the switch, and housing the dielectric (currently SF_6). Initial designs had the laser entering vertically as is typical at SNL,

9
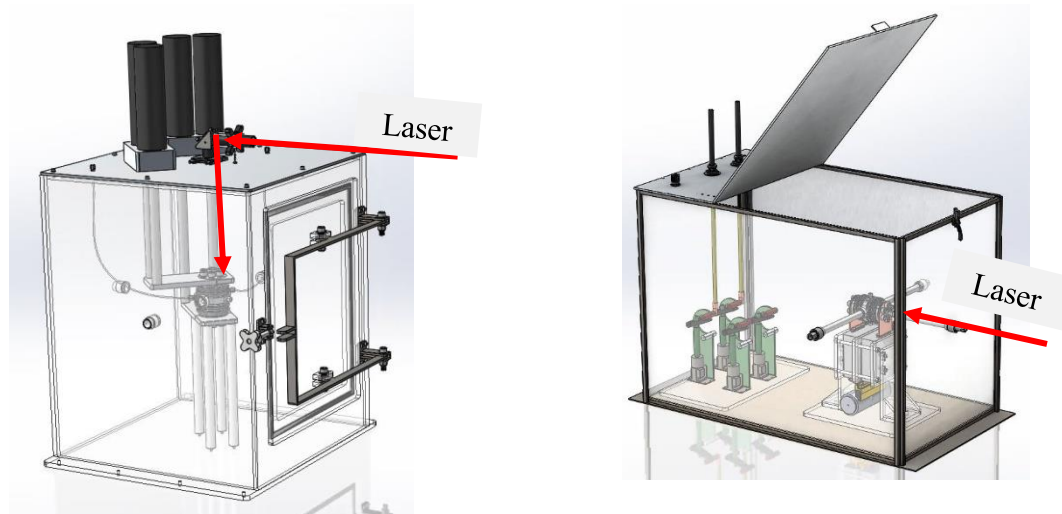
Figure 2-2: Left: Earlier design version bringing laser in from the top. Right: Final design with horizontal laser path

but a horizontal configuration was ultimately adopted (Figure 2-2). The final design allows maintaining coverage of all exposed HV equipment with gaseous dielectric, while still allowing open beam paths necessary for laser triggering and diagnostics (Figure 2-3). Further, the tank is designed to support the HV-LTS (provided by SNL) directly on top of the capacitors minimizing loop inductance. This configuration has the added benefit of maintaining the optical alignment when the switch is removed and re-installed.

The capacitors are connected via a high-quality current viewing resistor (CVR) that allows for measurement of the voltage, and subsequent current, during switch closure. Moreover, this low inductance short circuit design allows for determination of key electrical characteristics like equivalent circuit resistance and inductance. High voltage is brought in through the top of the tank by two 30 Ω cables that pass down to two sets of SNL provided Ross relays before attaching to the HV-LTS. Switch tank manufacturing utilizing a lightweight steel frame and ¼" acrylic for the walls. All acrylic was liquid welded together while held in clamps, then a steel frame was built around this. The tank was then outfitted with an aluminum (ground plane) lid that was drilled and tapped to accept a piano hinge that attaches the front and rear panels (Figure 2-4). A physical barrier was designed to keep the HV, pressure, and laser equipment away from the operator while
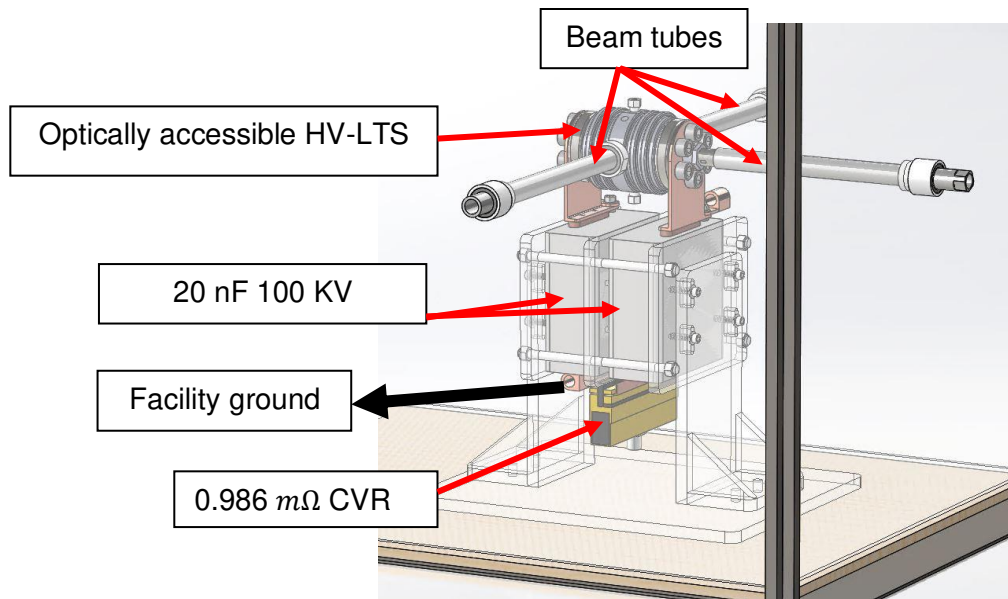
Figure 2-3: Capacitor and HV-LTS "brick" design operating in a short circuit configuration. The beam tubes on 3 sides are used to bring in the trigger laser as well as allow for diagnostic packages to be installed.

the experiment is in operation. Consulting NFPA 70e, the <u>limited and restricted approach boundaries</u> for this electrical system (+/- 125 kV = 250 kV) were determined to be <u>11' 3" and 5' 3"</u> respectively. Situated just outside the restricted approach boundary (Figure 2-1, left), and once the experiment is energized, the operator resides behind this barrier as the experiment can be run remotely. The barrier consists of two 8' tall by 5' wide wooden structures with an acrylic window to view the experiment safely. Accompanying the physical barrier is an associated lockout/tagout (LOTO) procedure that is presented in section 2.3.4. This LOTO procedure calls for a second person to be in the room, behind the barricade for the entirety of the procedure, and the circuit to be locked out can be seen in Figure 2-5. A high-quality shorting stick was procured from Mitchell Instrument that is rated for the operating voltages and stored energy. Only qualified personnel that have the requisite safety training are allowed to make access the HV system, including LOTO or maintenance.
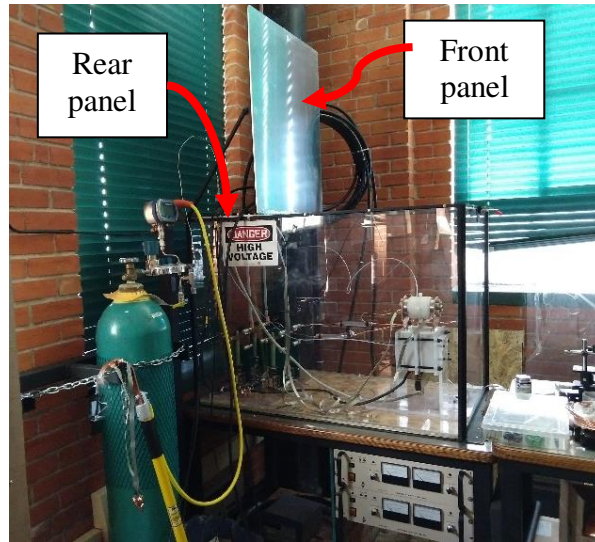
Figure 2-4: HV-LTS tank finished and installed with aluminum ground plane. Note the rear panel is attached to tank while the front panel hinges allowing for access to equipment

2.3 Delivery and Containment

2.3.1 Electrical

The electrical circuit used for this experiment consists of two high voltage power supplies capable of providing +/- 125 kV (Glassman WK series PS/WK125P5.0-11) through two 30 Ω cables. Electrical energy is switched through two sets of Ross relays (40 kV-air). Following the relays are two copper sulfate (CuS04) liquid charge resistors that are attached to two 20 nF, 100 kV liquid capacitors. Charge resistors were primarily used (Figure 2-5) to mitigate HV dump to ground in the event of a self-break during charging. Connecting the top of the capacitors is the optically assessable HV-LTS with 2 optical axes (4 ports), while the bottom is attached to a (CVR), yielding a short circuit configuration. All exposed electrical components reside inside an acrylic tank filled with SF_6 which greatly increases the dielectric strength[29,30] while allowing an optically clear beam path for measurements.
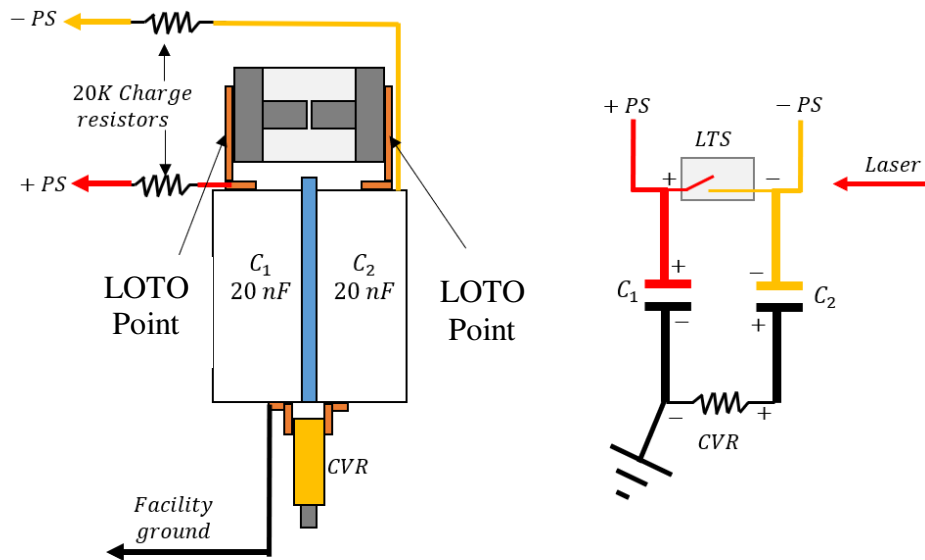
Figure 2-5: Left: circuit detail. Right: Current circuit setup. The entire bottom of the circuit is held at facility ground such that there is no need to short across both ends of the capacitor to prevent energy redistribution.

The relay circuit interior to the HV switch tank is designed to default to a mechanically safe position (Figure 2-6, Left). Relay 1 has its central (pivoting) node held at facility ground and the topmost node connected to the power supply. This relay design creates a default safe mode of operation such that node 1 and 2 are held together mechanically when the relay is powered off. Relay 2 has its topmost node tied to the switch through a high resistance charge resistor and its central node tied to the top node of relay 1. When the user wishes to charge the system, relay 1 must be powered up, removing the interlocking ground, and allowing the charge to pass through relay 2 and on to the switch. Then after the charge is complete, the operator powers relay 2 putting the circuit into isolation with its surroundings. Allowing for remote control of the experiment, a rack mount control box was manufactured to actuate the 110 VAC relays, control the interlocks, house an auxiliary power supply, and provide other features (Figure 2-7). The control box was built such that any exposed conductors were below 50 VDC, and the 110 VAC relays are plug and cord. Mounted on the front panel is a 10 A current limiting fuse in the event of a short circuit. Internal to

13

the control box is a custom external control board. Accepting a low current 5 VDC signal from an outside source, this external control board actuates the 110 VDC relays and controls the pressure system, power supplies and laser. The relay control box was primarily made to be externally operated (slave configuration) via a master control box (MCB). This MCB was built around an Arduino Mega 2560 (Figure 2-8) and is equipped with an on-board SD card that records operational data logs while the experiment is operated. Further, this unit can communicate with an auxiliary control box that logs data and sends it back to the MCB. For example, the auxiliary control box is responsible for firing the trigger laser. The MCB was programmed inside of Arduino's integrated development environment (IDE), and includes the ability to run in fully manual, semi-automatic and fully automatic modes. The fully automatic mode is currently capable of running through a single charge-fire cycle while future versions will be able to set the pressure and run multiple charge-fire cycles without user input.
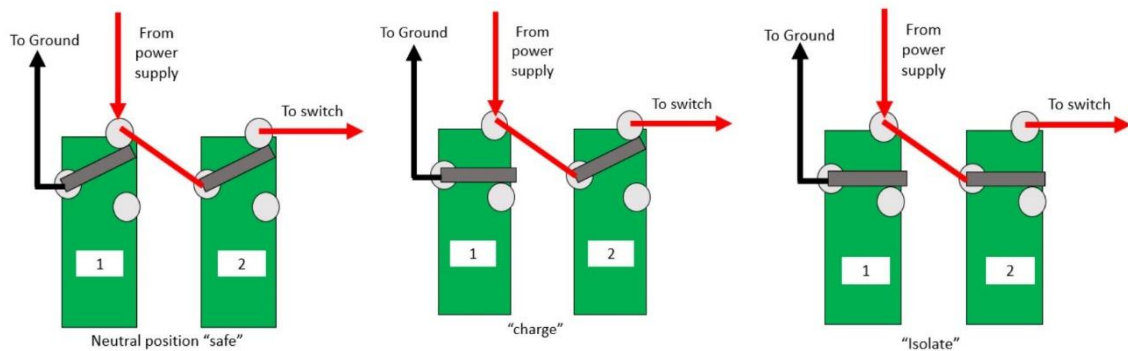
Figure 2-6: Left: Relay system in "safe" ground state, note this is mechanically neutral state. Middle: Relay 1 is dropped allowing for the HV-LTS to be charged. Right: Both relays are dropped putting the system into electrical isolation

Figure 2-7: Left: inside of the relay control box note the green board is the external control board. Right: the exterior of the control box.

Figure 2-8: Left/right: Open and closed views of the master control box centered around the Arduino Mega 2560 (left blue square). There are 3 I/O ports on the side of this unit accepting a 9-pin connector as well as an SD card slot for data collection

2.3.2 Pressure

Bottle management was designed to hold two 300 size cylinders. Retaining the gas bottles are two sets of chains that keep the bottles safely in the rack and the rack itself is fastened to the main structure of the experiment. Further, the pressure system necessary to operate the HV-LTS must allow an operational pressure (OP) high enough to achieve the desired percentage of self-break. Given the switch volume is small (and the system will operate with a low repetition rate) we utilized a regulator with a relatively small flow coefficient (C_v). From previous experiments on a similar HV-LTS, we know an OP of ~500 PSIG is adequate and a pressure system was built around this OP. See appendix A for associated pressure calculations and components.

2.3.3 Laser

The laser is inside an enclosed opaque acrylic enclosure with a single beam tube exiting one end facing the HV-LTS (Figure 2-9). Considering the laser is a pulsed Nd:YAG operating at the fundamental 1064 nm with a pulse width ~7-10 ns and a maximum output energy of ~50 mJ, laser safety goggles rated at OD 7+ (at the operating wavelength) are required when any beam is exposed. Moreover, operators must have passed laser safety training before being allowed to align or modify the laser system. Once any alignments are finished, the laser box is closed, and the beam tube is installed such that the laser is fully contained. While in normal operation, the laser, power supplies, and pressure system are controlled externally. Thereby keeping any need to enter the back half of the lab reduced as much as possible, excepting to change the laser energy. Laser plasma formation and switch triggering is achieved by an Nd:YAG (Big Sky Ultra CFR) with parameters as given above. This high energy laser beam is passed through a vacuum spatial filter (VSF) that cleans the transverse mode quality to M^2~1.25 before being expanded through a Galilean telescope. The purpose of this telescope is to set the beam diameter entering the final focusing element into the HV-LTS focusing down to a spot size on the order of 10-20 μm.

16

Laser pulse (timing) waveforms are collected from reflected light off the VSF with a fast (1 ns rise time) photodiode (Thorlabs DET-10A) and a Tektronix digital Phosphor oscilloscope (5 GHz).

2.3.4 LOTO Procedure

1) Prop open the main door, this will interlock the power supplies and laser if in operation.

2) Manually shut down the power supplies (large yellow button on front), and laser (key switch).

3) Turn off the high-pressure air and SF_6 bottles, then bleed off any pressure left in the high-pressure circuit by opening the pressure relays and manual ball valve that is before the PRV, as well as, the SF_6 circuit (open needle valve on regulator)

4) Check to make sure both the high pressure and low-pressure side of both the regulators are empty, attempt to increase the pressure on the regulators with the purge ball valve (high pressure) and needle valve (SF_6) full open. This ensures the entire switch and flowlines are empty

5) Depress the E-stop, remove and lockout the HV/laser power rail then place key in desk.

6) Install lockouts on both the zero air (300 size bottle) and SF_6 (80 size bottle) lines. Place the keys in the desk together with keys from step 5

7) Test to make sure the pressure system is empty by opening the pressure relays (high pressure air), and needle valve (SF6)

8) Test to make sure the HV system is off by attempting to turn on both the + and − power supplies with orange power ON button and the green enable button.

9) Test to make sure the laser is inoperable by attempting to turn it on, both by the key on the front panel and the laser ON button.

10) Find volt meter in desk and test on known condition to ensure it is operational.

11) Check, with volt meter, that shorting stick has below 1 ohm of resistance from ground point to facility ground.

12) Re-check volt meter on known condition to ensure previous measurement is reliable.

13) Connect one end of two shorting straps to the ground point of the shorting stick and the other to the facility ground lug on the switch tank.

14) Open the switch tank and hold the lid in the open position with the installed hardware.

15) While holding the short stick behind the rubber ring touch off on the + terminal on the top of the HV-LTS, hold for 5 seconds, remove the short stick and re-apply for 5 more seconds.

    a. Note the bottom of both capacitors is held at facility ground.

16) Repeat step 16 for the – terminal.

17) Move back to the + terminal and, while holding the short stick firmly against the + terminal, attach the shorting braid clamp to the + terminal.

18) Repeat step 18 for the – terminal.

    a. At this point there should be one ground braid attached from the ground plane to the + terminal and another to the – terminal at the LOTO points in Fig. 2-5.

19) Replace the shorting stick to its holding position, LOTO procedure is now complete.
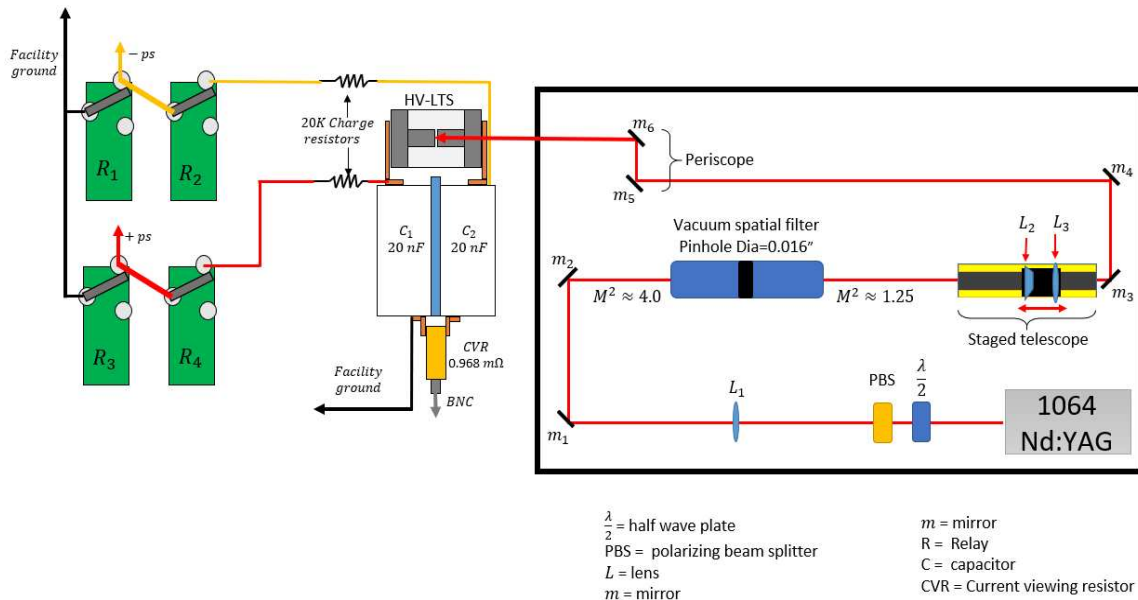
Figure 2-9: Notional HV (Left) and Laser (Right) components necessary to drive a HV-TS.

3. <u>Diagnostic Setup and Measurement Techniques</u>

3.1 Electrical Diagnostics

3.1.1 High Voltage Measurement

Given kV potentials and ns timescales, a direct contact (capacitive) measurement of the full voltage was not possible. Typical pulsed power machines utilize the so-called V-dot which is a non-contact measurement based on an inductively coupled device, essentially an antenna. V-dots require the voltage waveform travel through a pulse forming transmission line and considering this experiment has no transmission lines this was not an option. Ultimately, a CVR placed in series with the circuit was chosen that could withstand the power dissipation of the device and still allow a fast reading. Therefore voltage, and current, waveforms were measured by probing the CVR between C_1 and C_2 (Figure 2-9) and utilizing a 20-dB attenuator (Mini-Circuits HAT-20+) at the oscilloscope (Tektronix digital Phosphor oscilloscope 5 GHz). Data lines were produced in house and were equipped with an external stainless-steel ground braid to reduce the electro-magnetic interference (EMI) produced upon switch closure

3.1.2 Electrical Measurement Definitions

Common HV-LTS electrical characteristics include switch run time, 10-90 rise time and jitter. While the 10-90 rise time is a standard parameter computed from the time difference between the 10% and 90% marks of the voltage (or current) waveform (Figure 3-1, top), the switch run time and jitter lack standard definitions. In an effort to standardize the switch run time and jitter, we have defined the switch run time as the time delay between the time the peak of the laser pulse enters the switch to the time when the voltage (or current) waveform reaches 5% of its peak level (Figure 3-1, bottom). We define jitter as the standard deviation of the switch run time. The rationale for this is that the switch run time should only be a property of the switch, not the circuit or trigger laser. For example, if one defines the run time as some percent of the rising edge or the peak of

19

the initial trigger laser to the 5% mark of the current the run time would be a function of the laser pulse width and/or time of flight offset (Figure 3-1, bottom). Moreover, if more than the 5% mark of the current was used (as the ending time stamp) then the surrounding circuit electrical characteristics (e.g. inductance) would influence the run time. Further, jitter is, at times, defined as the maximum difference found among run times, but we feel that the standard deviation is more representative and less prone to outlier errors.

An important characteristic of all HV-LTS's is their self-break behavior. Essentially, when the applied field stress becomes sufficiently high, due to high voltage, the switch will spontaneously arc across like a lightning strike[4,11,28]. Gap spacing, electrode shape and material, fill gas and pressure, and applied voltage are all associated with self-break characteristics. Further, the percentage of self-break used in this work is defined as the ratio of the set voltage, to the voltage
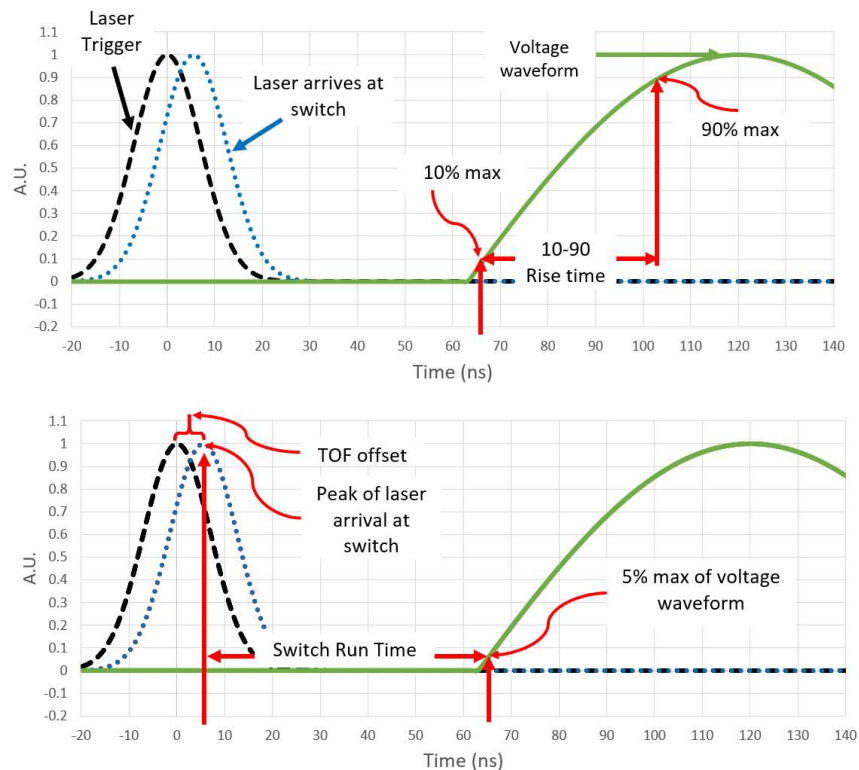
Figure 3-1: Definitions of electrical measurements including 10-90 rise time (Top), switch run time, and jitter (Bottom).

20

at which the switch will spontaneously arc across. Therefore, successful operation at lower percentage of self-break is considered favorable (to be further from spontaneous breakdown).

Electrical and optical measurements were carried out for various conditions including: percentage of self-break, fill gas type and pressure, laser location and energy, and electrical polarization (i.e. orientation of + and – terminals relative to the laser propagation direction). Laser locations were set qualitatively by eye (uncertainty ~+/- 1 mm) with location 1 corresponding to placing the laser on the surface of the downstream (opposing) electrode, and location 2 approximately in the center of the gap. Electrical polarization was defined as "normal" for the case where the anode is on the downstream laser side (where the beam is finally incident) with cathode on the upstream side (with laser passing through it), and "backwards" when the electrode polarities are opposite from that just specified, as per typical pulsed power standards (Figure 3-2).
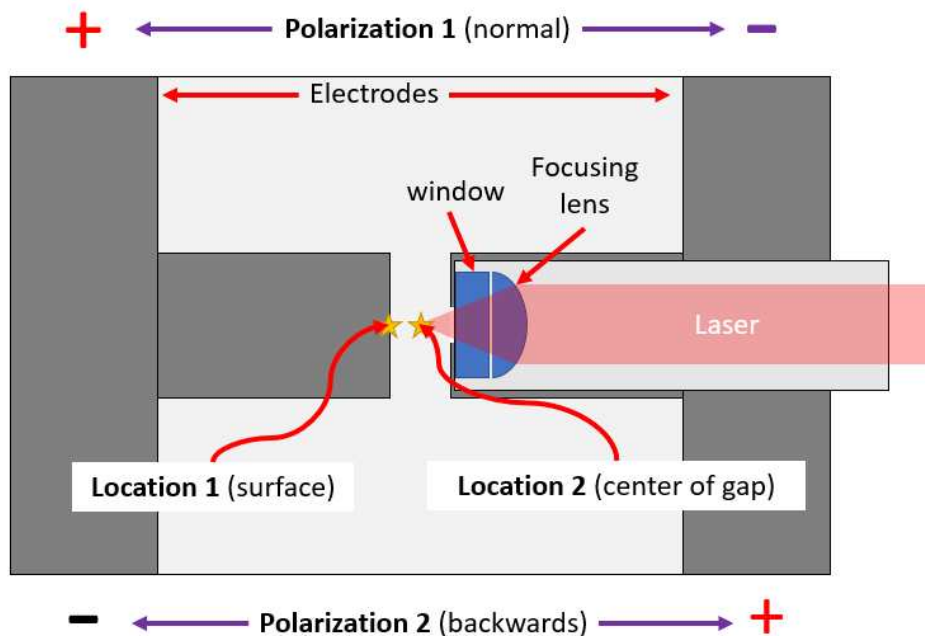
Figure 3-2: Layout of laser beam in optical switch and figure to illustrate definitions of Polarization and laser plasma location. See text.

3.2 Optical Diagnostics

3.2.1 Schlieren

Visualizing shock phenomena was accomplished by a Schlieren imaging system based off our previous work[31] and published literature[32,33] (Figure 3-3). Background illumination was provided from a He:Ne laser (Thorlabs HRP050 632.8 nm) that was expanded through a telescope (Lenses L_1 and L_2) from a starting diameter of ~0.8 mm to final diameter of ~4 mm. The collimated beam passes through the optically accessible switch and is focused by a long focal length lens (L_3). This lens was selected in conjunction with L_4 to produce a magnification of the central interrogation plane inside the switch by a factor of 4. A standard knife-edge was placed on a translation stage at the focus of L_3 and adjusted until uniform illumination was achieved. A bandpass filter (Thorlabs FL632.8-3, FWHM=3$\pm$ 0.6 nm) rejects other light (strong plasma luminosity) prior to imaging with a gated ICCD (Princeton Instruments PI-MAX: 1300) that was controlled externally (WinSpec 32), and timed relative to the arrival of the initial laser trigger pulse
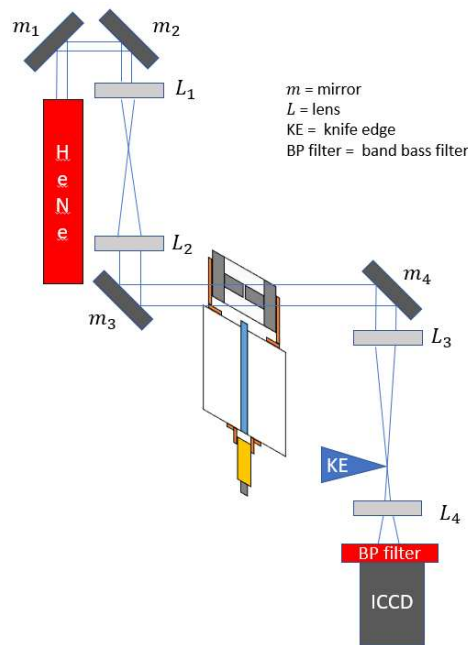
Figure 3-3: Schlieren imaging optical train consisting of a red He:Ne, standard visible coated lenses, matched band pass filter, and gated ICCD.

via a delay generator (SRS DG-535). This optical train was designed to produce a real image on the ICCD array (operated without objective lens).

3.2.2 Optical Emission Spectroscopy (OES)

We have developed setups for both 1-D (spatially-resolved) OES along the switch axis (trigger laser direction), and 0-D (non-spatially resolved) OES (Figure 3-4). The 0-D "pointwise" design incorporated a 400 mm (L_1) lens to collimate the plasma luminosity, which was then sent to a 300 mm lens (L_2) matching the f# of the monochromator (Princeton Instruments SP-2300i). Considering the slit orientation of the monochromator was orthogonal to the plasma channel, a periscope was installed to rotate the orientation accordingly. The same gated ICCD (PI-MAX: 1300) was coupled to the monochromator and used for schlieren imaging. 1-D spatially resolved spectra were measured by collecting the emission light with a 7 X 200 μm linear fiber array (Thorlabs BFA200HS02) with an achromat doublet lens (L_3) on the downstream end matched to the numerical aperture (NA) of the monochromator (Figure 3-4, right). This optical train was designed to achieve a 2:1 demagnification of the plasma channel diameter referenced to the optical fiber. After installing the optical components, the fiber was backlit, and a beam profiler was installed at the central axis of the HV-LTS, where the final alignment was accomplished by bringing the real image of the fiber into focus (Figure 3-5). In this way, the actual spatial extent of the fiber was found to be 3.13 mm with each fiber covering ~0.45 mm yielding a length very close to that of our gap.
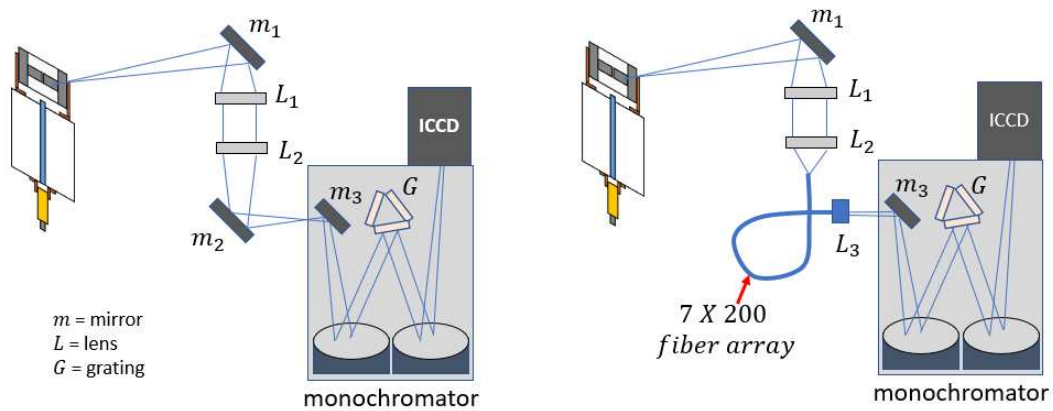
Figure 3-4: Left: 0-D spectroscopic optical design. Right: 1-D (spatially resolved) optical design
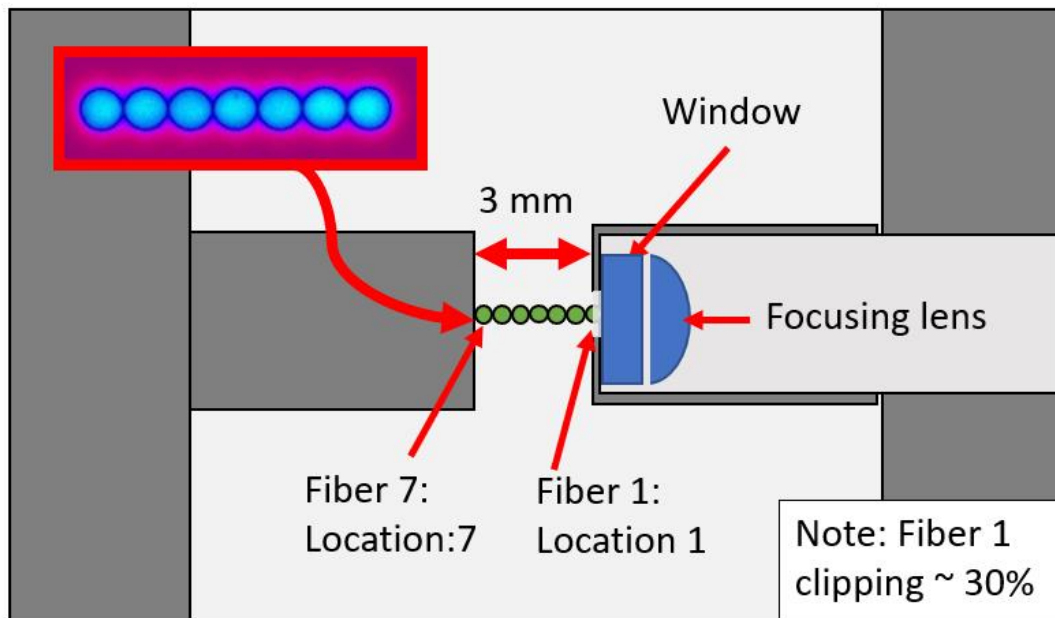
Figure 3-5: notional geometry of HV-LTS, with backlit 7 X 200 um liner fiber array focused on central plane of the switch seen in green spanning the gap. Inset image is from beam profiler of alignment from backlit fiber

24

4. Results and Discussion

4.1 Electrical Characterization

4.1.1 Self-Break Limit

The self-break voltage values (Figure 4-1) of the optically accessible switch were determined for dry zero air and SF_6 as a function of fill pressure. The voltages were found fixing the switch pressure then slowly increasing the voltage until the switch spontaneously closed (i.e. until current flowed). This was repeated 10 times for each data point (gas type and pressure) and averaged. Given the electrical system can bias the switch with different voltages across the two electrodes, data reported here have employed equal voltages (of opposite polarity) over both electrodes (with the reported value being the difference between the two electrodes). Self-beak data presented are in good agreement to those found from previous experiments at SNL[15] for dry air.
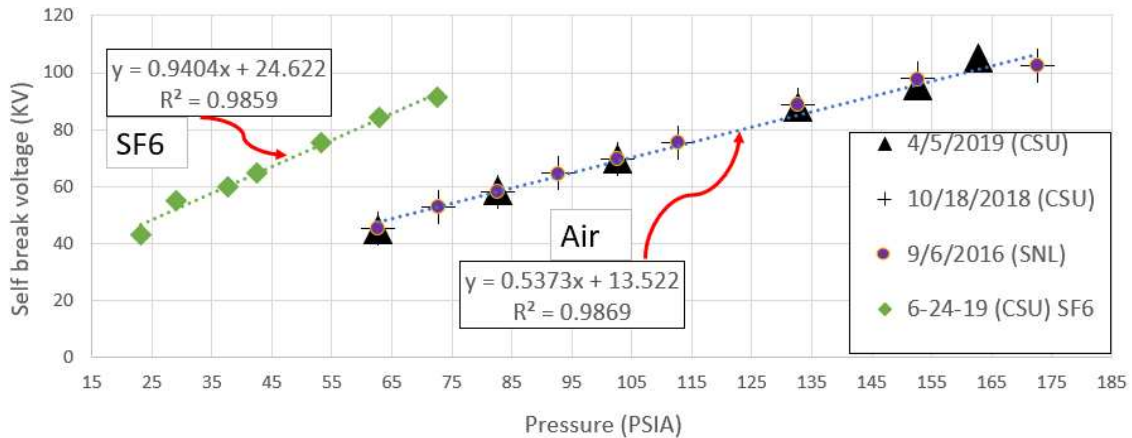
Figure 4-1: Switch self-break voltages for dry air and SF_6. In laser triggered experiments, these values are used to determine the % of self-break as lower applied voltages are used.

4.1.2 General Switch Behavior

Considering the switch fires into a short circuit (Figure 2-5), the output voltage waveform was observed as a damped ringing sinusoid (Figure 4-2). Moreover, the rise time, periodicity, and exponential decay of the output waveform can be analyzed to determine electrical characteristics including equivalent circuit resistance and inductance (discussed in Section 4.1.5). Plasma luminosity was measured with a photodiode (Thorlabs DET-10A) and found to increase monotonically until a peak with timescales being driven by the set voltage. Specifically, 25-kV shots were found to peak out at ~ 200 ns and 50-kV peaked at ~ 500 ns (Figure 4-2) relative to laser pulse arrival at the HV-LTS. Long-term decay of the current, and subsequent luminosity was observed to occur over a time span of ~4-5 μs (Figure 4-3) and this behavior was consistent over all voltages evaluated. Note, considering the periodicity and exponential envelope of the CVR signal is defined by the equivalent circuit resistance, inductance, and capacitance, only one CVR trace is shown for Figure 4-2 because when normalized the 25 kV and 50 kV data are essentially identical. Moreover, all data was lowpass filtered then spline fit in order to compute the switch characteristics like run time, 10-90 rise time, etc. Therefore, the temporal resolution of the photodiode and electrical data is set by the fidelity of the lowpass filter and spline fit, rather than the sample rate of the scope, given enough points to resolve specific features.
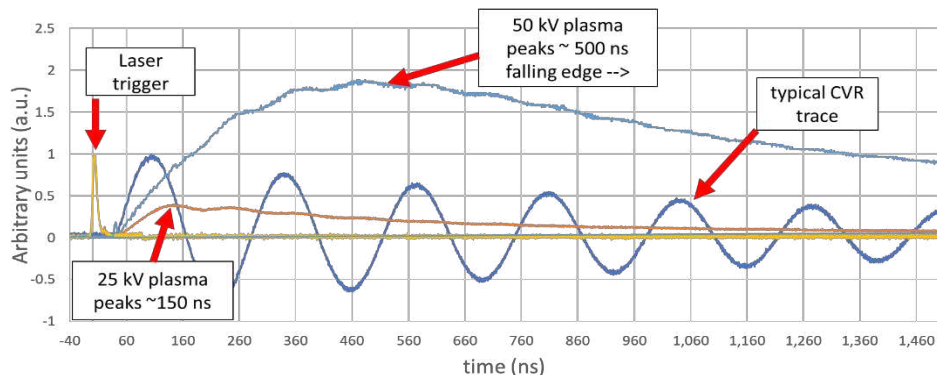
Figure 4-2: Typical current and plasma luminosity. Current was measured from a CVR with a known resistance, and luminosity was measured with a photodiode (Det10A).

26
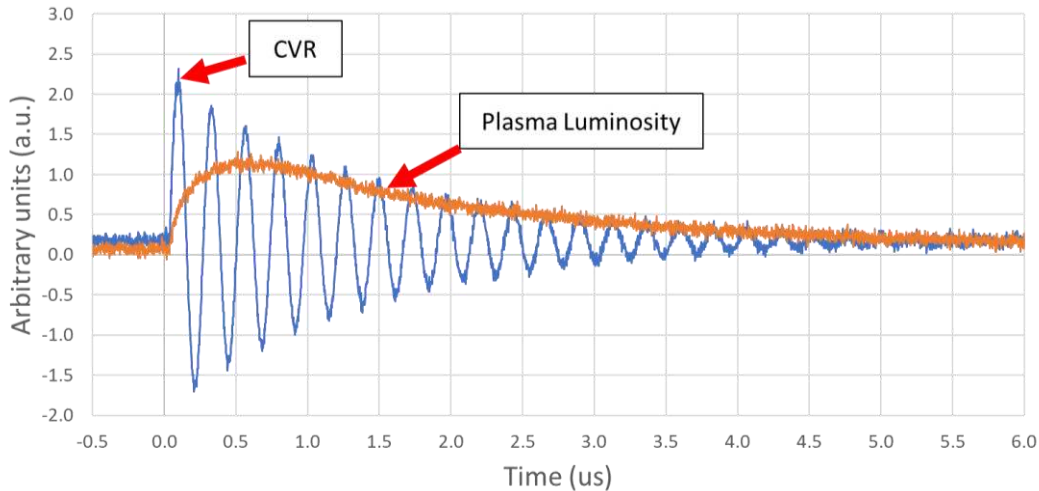
Figure 4-3: Long term switch electrical behavior. Note the amplitude of the oscillations depends on the set voltage. but the frequency and decay time is essentially constant and an intrinsic characteristic of this circuit.

4.1.3 Run Time and Jitter

Switch run time and jitter were determined for a range of input parameters. Specifically, the design space for current experiments spans 2 laser locations, 3 voltages, 3 percentages of self-break, and 2 fill gasses, with 3 shots being averaged for each data point. Every possible permutation was not tested, instead the differences of laser location, electrical polarization, and fill gas were determined to be paramount and the final experimental matrix was created with this in mind. The most favorable laser location with respect to run time (i.e. that yielding the shortest run time) was found to be when the laser plasma was on the electrode surface (i.e., at location 1, Figure 4-4) for normal polarization. Previous data has shown that for backwards polarization switch performance is very poor at location 1. Run times as low as 9 ns were observed with the laser in this location with jitter less than 1 ns for all runs (Figure 4-5). Switch performance with the laser placed at location 2 (i.e., center of gap) yielded higher run times and jitter for essentially every run regardless of polarization. Given that, for location 2, the laser is required to form a plasma in the gas phase, higher laser energies were necessary (compared to location 1) and switch performance was observed to be sub-par below approximately 4 mJ as evidenced by higher run

27

times and jitters in all tests. As the trigger laser energy was increased above 6 mJ (location 2), switch run times and jitter approached their minimum for essentially all runs. This makes intuitive sense and is true regardless of location as the laser produces a more intense plasma at higher fluences, switch behavior should tend to plateau with diminishing returns on improving runtime and jitter characteristics. Essentially, if the laser produces a plasma channel across the entire gap this would be tantamount to a dead short like a solid wire bridging the gap and a snap to approximately full conductance. At this point any additional laser energy will not increase switch performance (reduction of jitter or run time) as the switch will be naturally inductively limited by the driving circuit.

Electrical polarization was found to have a significant impact on the run time and jitter characteristics for both locations tested. Previous literature has shown that these HV-LTSs perform better when the laser strikes the anode[8,28,29] (polarization 1, location 1) and this is consistent with our findings (Table 1) On the other hand, focusing the laser in the center (location 2) we found that the run time and jitter characteristics are very similar for either polarization at higher laser energies. This behavior was found to be consistent for higher set voltages (above 50 kV) for dry air. The effects of fill gas were investigated comparing dry air and SF_6, a common gas used in other HV-TLS's[12,29,34], albeit typically utilizing a UV laser[7]. Overall switch performance was observed to be very poor for all conditions at location 2 (gap), and higher than normal laser
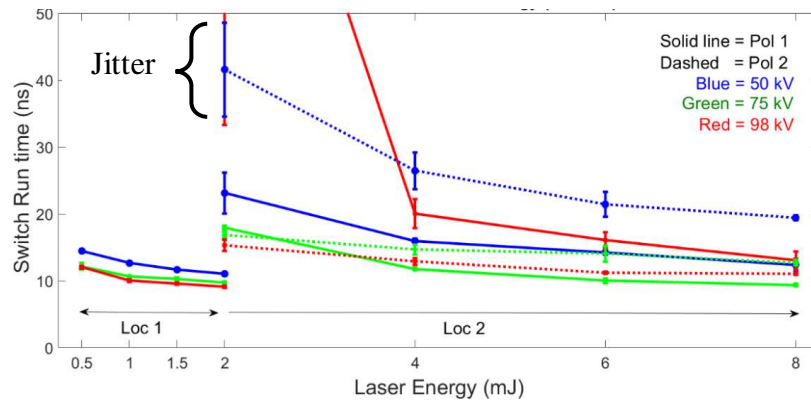
Figure 4-4: **Dry air** switch run time versus laser energy at 80% self-break.
Note, solid red line (98 kV Pol 1) for location 2 at 2 mJ is an outlier and should be ignored.

energies were necessary at location 1 (surface). Specifically, laser energies above 3 mJ were required to get full switch closure with rise times (Figure 4-5) and jitter considerably larger than the equivalent condition with dry air. Note, data presented represents averaging over 3-5 data points and is meant to show general behavior. Further experiments may home in on specific switch characteristics and larger data sets will be necessary to show statistical significance. Given small sample sizes, some of the data shown does not agree with the general switch behavior. Specifically, Figure 4-5 shows worse jitter at 98 kV than 75 kV for multiple laser energies, this is almost certainly not physical and only an artifact of small sample sizes. Moreover, 98 kV was chosen as the maximum voltage as higher set voltages yielded significant current shunting. This manifested itself as a large current draw above 98 kV, as well as, when the switch was isolated the time delay between isolation and laser fire yielded dramatic changes in run-time and jitter. Therefore, the time delay between isolation and laser fire was regulated by the MCB in section 2.3.1.
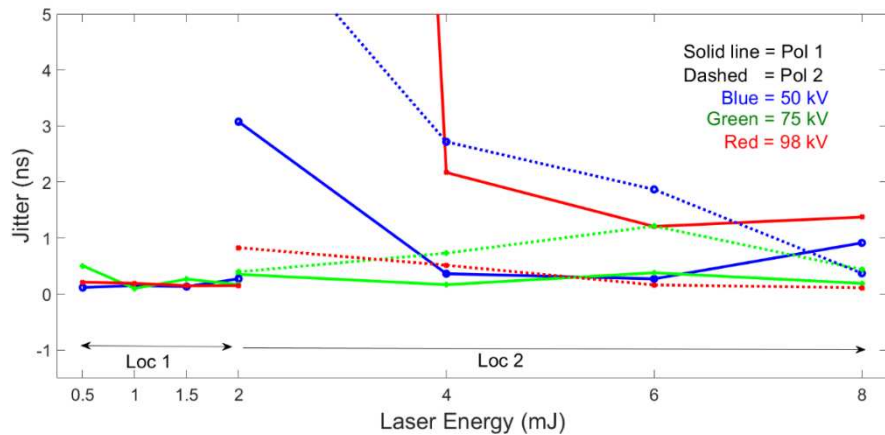
Figure 4-5: **Dry air** switch Jitter vs. laser energy at 80% self-break. Note, solid red line (98 kV Pol 1) for location 2 at 2 mJ is an outlier and should be ignored.
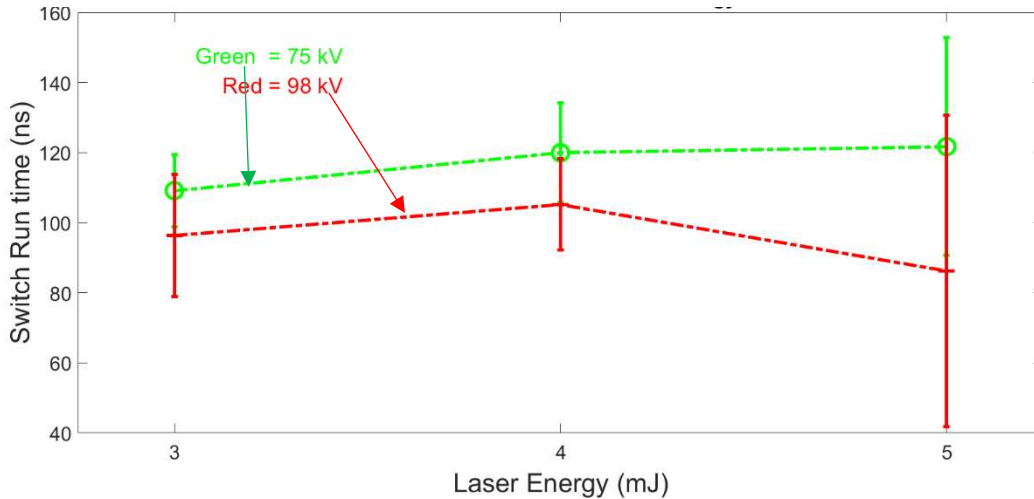
Figure 4-6: **SF6** Switch Run time vs. Laser energy, location 1 (surface), Polarization 1 (normal)

4.1.4 10-90 Rise Time

Switch rise time is an important characteristic of a HV-LTS and is indicative of the greater driving circuit feeding the switch. A switch with high inductance will have a slow rise time and a switch with low inductance will have a fast rise time. Calculating switch rise times for the test matrix summarized in Table 1, and plotting against laser energy, one finds that the rise time is essentially unaffected by the laser energy (as long as it is high enough to trigger the switch in the first place). However, plotting against percentage of self-break we observed run times grouping as a function of set voltage. Note to achieve a constant percentage of self-break the voltage was fixed, and the pressure was adjusted for each set voltage. For the surface location (1) and normal polarization (1) we observed the 50 kV data having the slowest overall rise times, with 98 kV in the middle and 75 kV having the fastest rise times (Figure 4-7). Keeping the polarity the same and moving the laser to the center (location 2) this behavior persisted with the 80% of self-break showing distinct regions where the rise times tended to fall (Figure 4-8). Then, swapping the polarity (2) while maintaining all other variable constant this behavior was observed to flip for the 75 kV and 98 kV set voltages (Figure 4-9).

30
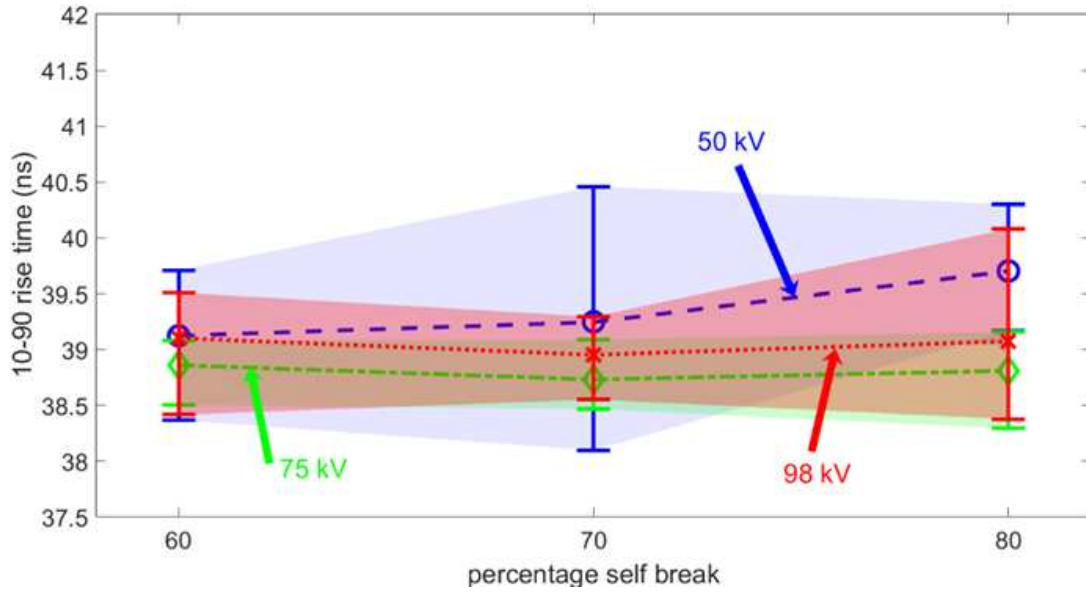
Figure 4-7: **Dry air**, 10-90 Rise time versus % of self-break for several applied voltages. **Location 1, polarization 1.** Four data pts. for each condition are due to different laser energies of 0.5, 1, 1.5 and 2 mJ
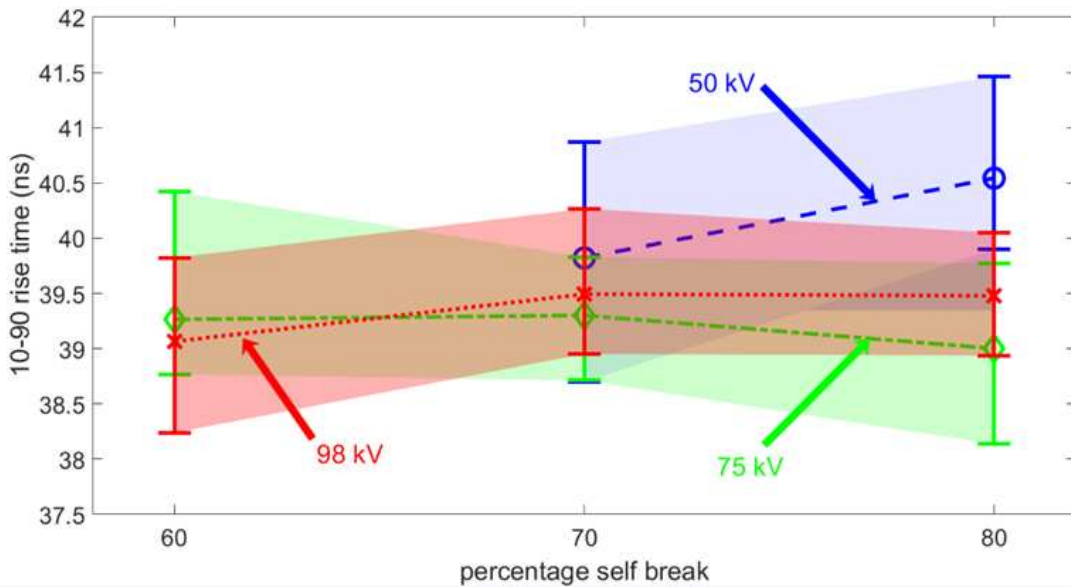
Figure 4-8: **Dry air**, 10-90 Rise time vs. % of self-break 50-98 kV. **Location 2, polarization 1.** Four data points per %SB relate to a laser energy of 2 to 8 mJ. Note, 98 kV data binning near the center of the data set for all % of SB
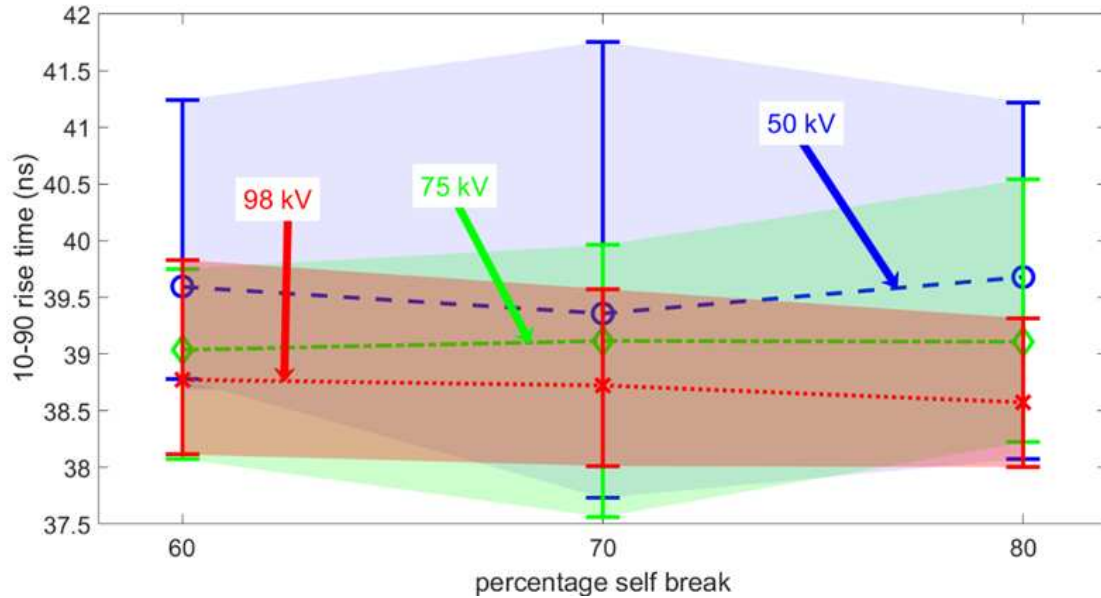
Figure 4-9: **Dry air**, 10-90 Rise time vs. % of self-break 50-98 kV. **Location 2, polarization 2.** Four data points per %SB relate to a laser energy of 0.5 to 2 mJ. Note, the relative locations of the 75 and 98 kV set voltages have swapped place with P2

4.1.5 Overall Switch performance

Overall switch performance was determined by evaluating the run time, jitter, and percentage of self-beak as a weighted average score. Before calculation of the weighted score all outliers were removed (run time > 100 ns), and all data was normalized to unity based off the local maximum in each data set. For example, location 1, polarization 1 each jitter data point was divided by the maximum jitter found (neglecting outliers) in this data set; in this way any unit conversions are accounted for. Weightings were assigned based off impact and three cases were considered to display differences in defined significance:

1. Jitter is sole interest in performance (Table 1)

    a. $J_W = 1$, $PSB_W = 0$, $RT_W = 0$.

2. Run time is sole interest in performance (Table 2)

    a. $J_W = 0$, $PSB_W = 0$, $RT_W = 1$.

3. Jitter is most important then % of self-break, then switch run time (Table 3)

    a. $J_W = 0.5$, $PSB_W = 0.3$, $RT_W = 0.2$

32

Where J_w is the jitter weighting, PSB_W is the percentage of self-break weighting, and RT_W is the run time weighting. The average weighted score was then calculated as:

$$Weighted\ score = J \ X \ J_W + PSB \ X \ PSB_W + RT \ X \ RT_W$$

Where J is the jitter, PSB is the percentage of self-break, and RT is the run-time. A weighted average was then calculated for each data point in all data sets. To directly compare electrical polarizations, location 2 (gap), polarizations 1 and 2 were then normalized again to the maximum found over these two data sets (maximum weighted average score). Note, this routine yields a set of data points where smallest is best. Finally, the weighted data is color coded to determine regions of best performance where solid green is defined as best, and solid red is defined as worst. Between these extremes a color scale is applied to visually see the switch performance depending on the assigned weightings.

Table 1: Overall switch performance with respect to switch

Combined weighted score											
	Location 1 (on surface)				Location 2 (In center of gap)						
Set Voltage (kV)	Polarization 1 ("normal")				Polarization 1 ("normal")				Polarization 2 ("backwards")		
	Laser mJ	% of self break			Laser mJ	% of self break					
		60	70	80		60	70	80	60	70	80
50	0.5				2		outlier				
50	1				4						
50	1.5				6						
50	2				8	Outliers					
75	0.5				2		outlier				
75	1				4						
75	1.5				6						
75	2				8						
98	0.5				2				outlier		
98	1				4	Outliers					
98	1.5				6						
98	2				8						
Key =>	Worst performance						Best performance				

Table 2: Overall switch performance with respect to switch run time

Combined weighted score

Set Voltage (kV)	Laser mJ	Location 1 (on surface) Polarization 1 ("normal") % of self break 60	70	80	Laser mJ	Location 2 (In center of gap) Polarization 1 ("normal") % of self break 60	70	80	Polarization 2 ("backwards") 60	70	80
50	0.5				2		outlier				
	1				4	Outliers					
	1.5				6						
	2				8						
75	0.5				2		outlier				
	1				4						
	1.5				6						
	2				8						
98	0.5				2	Outliers	outlier				
	1				4						
	1.5				6						
	2				8						

Key => Worst performance — Best performance

Table 3: Overall switch performance with weightings: $J_W = 0.5$, $PSB_W = 0.3$, $RT_W = 0.2$

Combined weighted score

Set Voltage (kV)	Laser mJ	Location 1 (on surface) Polarization 1 ("normal") % of self break 60	70	80	Laser mJ	Location 2 (In center of gap) Polarization 1 ("normal") % of self break 60	70	80	Polarization 2 ("backwards") 60	70	80
50	0.5				2		outlier				
	1				4	Outliers					
	1.5				6						
	2				8						
75	0.5				2		outlier				
	1				4						
	1.5				6						
	2				8						
98	0.5				2	Outliers	outlier				
	1				4						
	1.5				6						
	2				8						

Key => Worst performance — Best performance

34

4.1.6 Lumped Impedance and Resistance

Investigating more intrinsic electrical characteristics, lumped inductance and resistance were determined from data collected from the CVR. It was observed that this circuit's electrical characteristics were essentially unperturbed by either the set voltage or laser trigger energy, as long as the system successfully triggered. Calculated inductance and resistance values (see appendix B for details) were determined to be 136 ± 1 nH and 0.21 ± 0.01 Ω respectively (where uncertainty range is found as the standard deviation of individual measurements).

4.2 Plasma Channel Characterization

4.2.1 Radial Growth

Schlieren images were first collected from only the laser plasma in the switch with no external voltage. These images allowed a study of the blast wave produced by the laser generated plasma. Imaging was performed for cases with the laser focused on the surface of the opposing electrode as well as with the laser focused in the center of the gap. The pressure inside the switch was regulated to 220 PSIG corresponding to ~80% SB at 100 kV external voltage. Note: switch behavior depends on the absolute pressure in the switch which can be found by adding our lab atmospheric pressure (12 PSI). We implement a single-frame phase locked approach to "stitch" images given our ICCD was not capable of capturing multiple images from a single switch event. High speed images were acquired with camera shutter exposure times of ~20 ns. Timing data was collected and consisted of the laser arrival at VSF, laser arrival at switch, laser plasma generation, and camera shutter sync. This data was then analyzed allowing for precise time stamps of the event in question. Pixel intensities observed from pure schlieren, i.e. at later times with >255 ns in Figure 4-10 with no plasma luminosity were above the detector noise level, but only by a factor of ~5. Pixel intensities taken earlier during the laser plasma evolution were considerably higher, e.g. a factor of ~25 above the noise level at time delay of 15 ns. This light leakage of plasma luminosity is a consequence of the band pass filter width. Raw data output

35
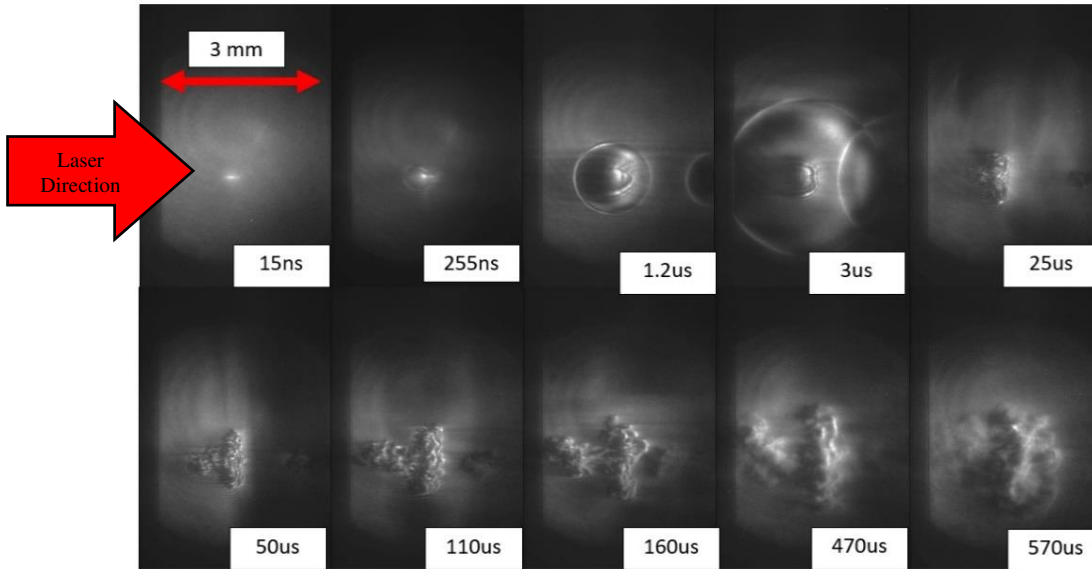
Figure 4-10: Schlieren images of the shock wave generated by ~ 4 mJ of laser energy deposited into 220PSIG ultra zero air. Note, Plasma luminosity can be seen in the top left figure.

from the controlling software (WinSpec 32) was imported into MatLab where stretching of the contrast allowed for visualization of the images and data analysis. The timeline and qualitative attributes of the laser plasma schlieren and shock wave images match with published literature. Specifically, the shock front propagation was observed to be spherically symmetric at early times and later the generation of the third lobe was observed at ~25 μs[26,31]. These data allow quantitative study of blast wave propagation, e.g., shock front detachment was observed to occur at ~500 ns for a laser energy of 4 mJ. Radial velocities before detachment (~250 ns) were determined to be order of 1000 m/s (or about a Mach 3 shock referenced to ambient conditions). At later times following detachment (~6 μs), the velocity of the shock rapidly decayed and stabilized to just above Mach 1 which is consistent with published literature[35,36]. Following the laser-only schlieren, we advanced to imaging of the laser plasma in the presence of external voltage. Owing to the more intense plasma, particularly when viewed at early times, the schlieren images also contain a "leakage" contribution due to plasma luminosity. Images were taken for voltages ranging from 25-100 kV. Given the presence of the plasma luminosity, these images can be used to extract data on radial plasma channel growth as was done for the 50 kV and 100 kV

36

cases (Figure 4-11 & Figure 4-12). Figure 4-13 shows complex plasma filamentation over the first tens of ns of the current pulse for both 50 and 100 kV cases. The nature of the filamentation, generally observed as having a trident of 3 filaments, will be further examined in the future including possible stochastic behavior of number of filaments and their attachment locations. Given the filaments, and with the goal of studying plasma column radial growth, all radial data presented have been determined at a fixed location 1 mm from the right electrode (Figure 4-11). Initial velocities of the plasma channel growth were observed to be on the order of Mach 10 for the first ~150 ns (Figure 4-12), After which, the radial growth started to decay. This data was fit with an At^k trendline (Figure 4-13) and compared to the scant published literature with decent agreement[12,17] of the exponential k factor, while having great differences on the pre-exponential A factor. Reviewing equation (3), the pre-exponential factor does not play into the governing equations for the Martin model while the k factor does. Therefore, given the temporal radial growth of the plasma channel follows equation (2) for the timescales of consequence (rising edge), we validate the plasma channel radial growth assumption used in the Martin model against data from Martin[11], Wolford[16], and in conjunction with data herein. Moreover,
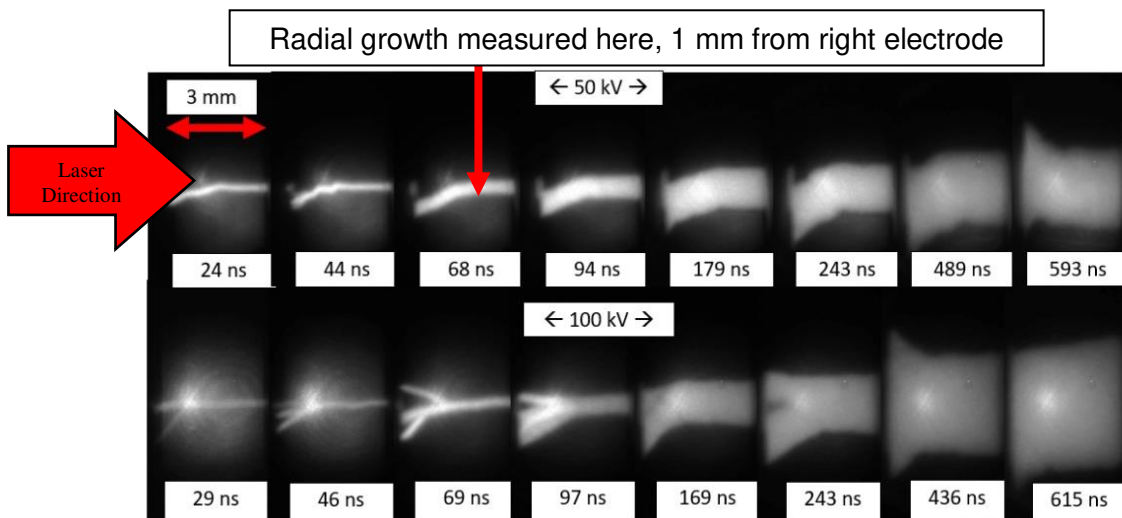
Figure 4-11: Schlieren images of the switch closure plasma channel evolution over the first 600 ns. See text

the consequence of the observed perturbation in the constant k then will only make minor perturbations in the ζ term (assuming k does not drop near zero), which only weakly perturbs the overall calculated plasma channel resistance. Specifically, calculating the maximum measured deviation of k (0.22=0.575/0.737) alters the overall plasma channel resistance by only ~ 15 % if all other parameters are held constant.
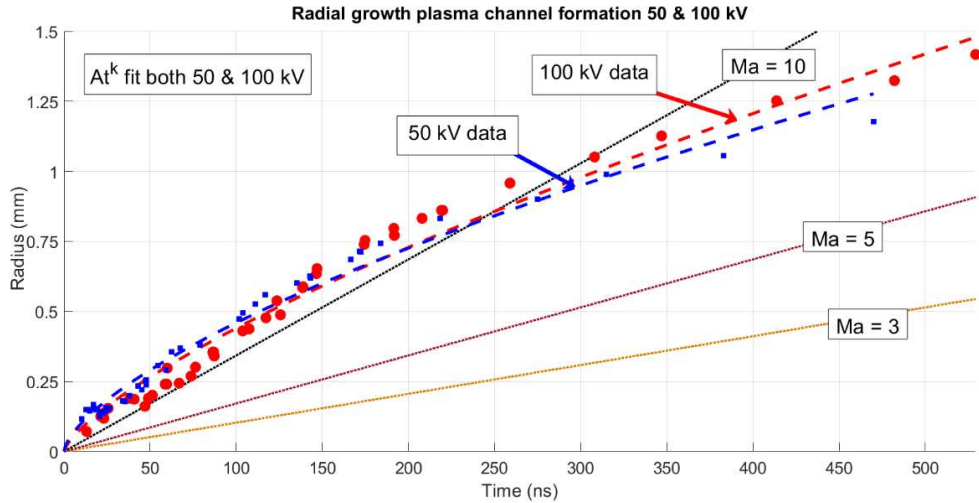
Figure 4-12: Plasma channel radial growth compared to lines of constant Mach. The velocity of the plasma channel growth is ~ Mach 10 for the first ~ 150 ns
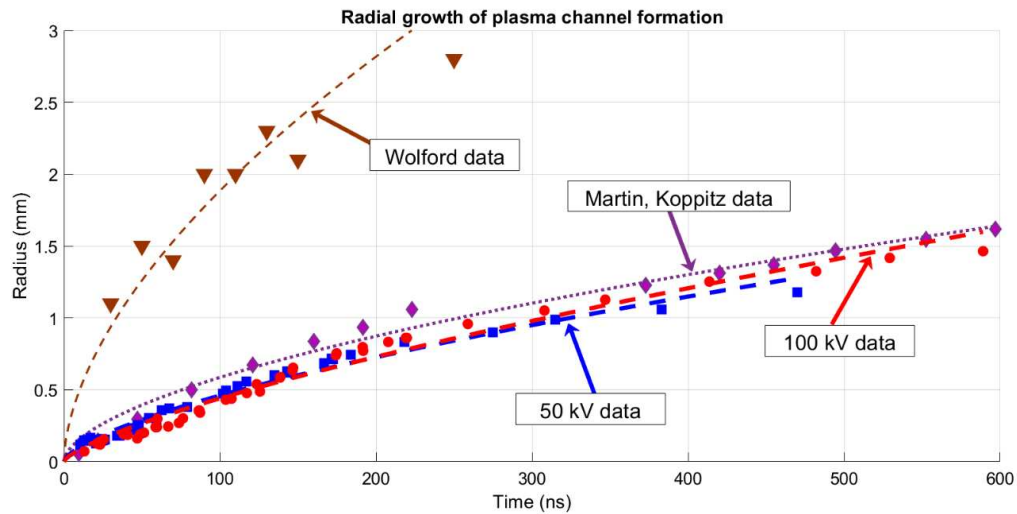
Figure 4-13: Measured radial growth fitted to equation (2) showing good agreement. Plotted along with [11, 16]

38

Table 4: Fit coefficients for Martin[11], Wolford[16], and current investigation. Fit over first 600 ns of data for At^k trendline

	A	k	R^2
Martin[11] Fig. 1	176.6	0.644	0.989
Martin[11] Fig. 13	6.242	0.575	0.983
Wolford[16]	21.75	0.580	0.974
Rose 50 kV	19.452	0.661	0.982
Rose 100 kV	54.23	0.727	0.974

4.2.2 Optical Emission Spectroscopy

OES data were taken for various experimental conditions to investigate plasma conductivity which is assumed constant in Martin model. Calibration of instrument line broadening utilized a He:Ne laser (632.8 nm) for several groove spacing's as shown in Figure 4-14. We found a minimum resolution of ~0.1 nm with the 1200 g/mm grating. Note: the non-monotonic dependence of wavelength resolution due to slit width is attributed to constraints in camera position and will be further examined. Wavelength calibration was performed over the region of interest using a fiber coupled mercury argon lamp from Ocean Optics (CAL-2000). A relative intensity calibration will be performed in the future. Probing low switch voltages (25 kV), a 0-D spectral survey was conducted to view general behavior (Figure 4-15) in the spectral region between 500 and 650 nm using a grating with 300 g/mm. During initial switch closure, no emission lines were observed, and the spectra tended rapidly toward continuum. Emission lines were not observed until ~ 170 ns after switch closure for this low voltage case (Figure 4-15, top). At later times, when the current started to decrease significantly, and the plasma cooled, individual emission lines appeared consistently (Figure 4-15, bottom). Following the initial pointwise measurement, a 1-D spectral survey was conducted, resolving the plasma luminosity over the 3 mm gap inside the HV-LTS. With knowledge from the 0-D test case, a central wavelength of 550 nm was chosen using a grating with 600 g/mm to view lines of interest. Spectra were collected for 30 and 50 kV cases

(Figure 4-16 & Figure 4-17). Location assignments (relative to the electrodes) were made with "location 1" corresponding to the upstream electrode (to the right images and through which the laser enters), and "location 7" being the opposing electrode (left). Reviewing data for the 30 kV case (Figure 4-16) on the rising edge of the plasma luminosity (Figure 4-2), no emission lines were visible until delay of 219 ns for all locations (Figure 4-16, top). Locations 1, 2, and 7, near the electrode edges, generally show lower overall intensity relative to the central section of the plasma (locations 3-6). For the 50 kV data (Figure 4-17), the plasma luminosity trended toward continuum during early times (rising edge of current trace) with spectral lines not observed until ~500 ns, much later than the two previous tests. These data are informative as to the time delays under which line emission is visible and line-based OES methods, such as Boltzmann and Stark analyses, may be used to study the HV-LTS including examining assumptions of the Martin model. Initial line assignments are shown in Figure 4-18 for later times from the 30 kV spatially resolved data. Assignments were made by reviewing the National Institute of Standards and Technology[37] (NIST) database for known spectral lines of atomic nitrogen and oxygen including neutrals, single, and double ionization states.
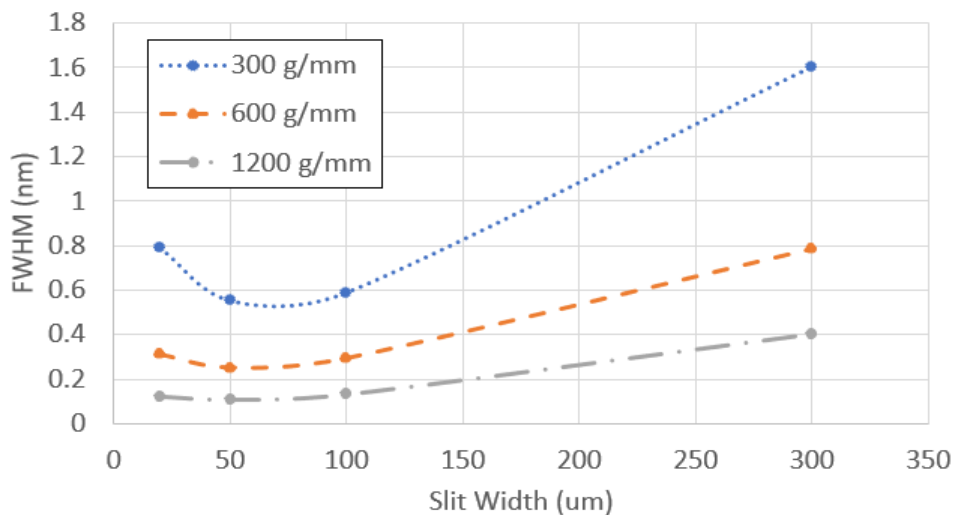
Figure 4-14: Instrument line broadening using a narrow line width He:Ne (632.8 nm) laser
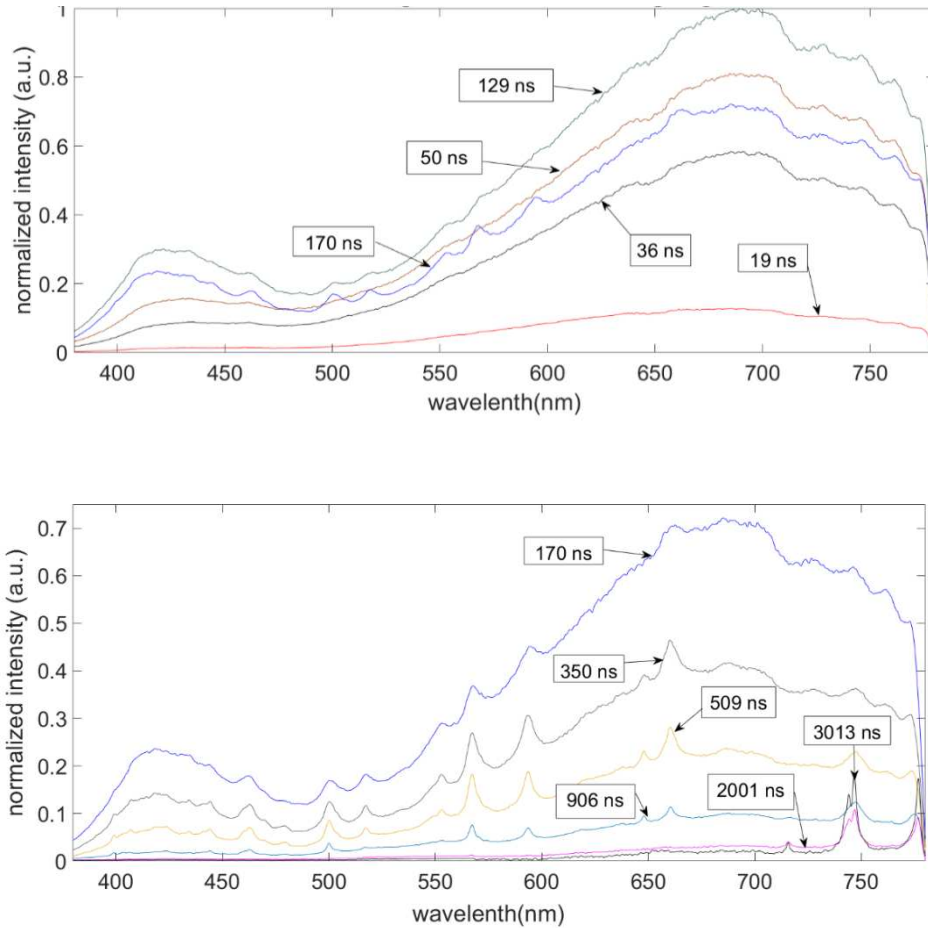
Figure 4-15: Top: Initial low voltage (25 kV) survey plasma spectra for the rising edge of the plasma luminosity. Bottom: same as top but for later times on the falling edge of the current pulse. At later times for the 700-800 nm range neutral nitrogen and oxygen lines start to appear (~ 2000-3000 ns)

41
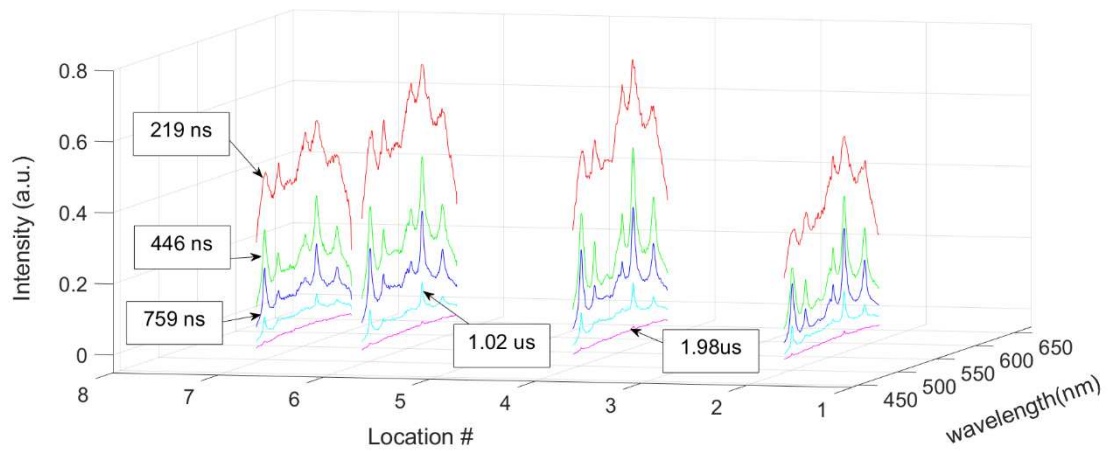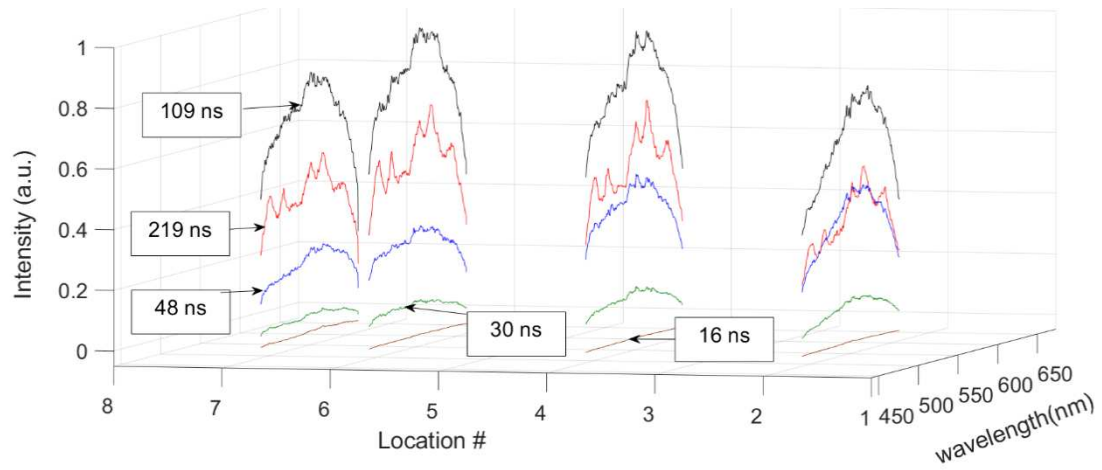
Figure 4-16: Top: 30 kV spatially resolved spectra on the rising edge of the plasma luminosity. Bottom: same as top but for later times on the falling edge. Locations 1, 3, and 5 have been removed to better view nearby spectral evolution. These locations have consistent spectral behavior as surrounding locations
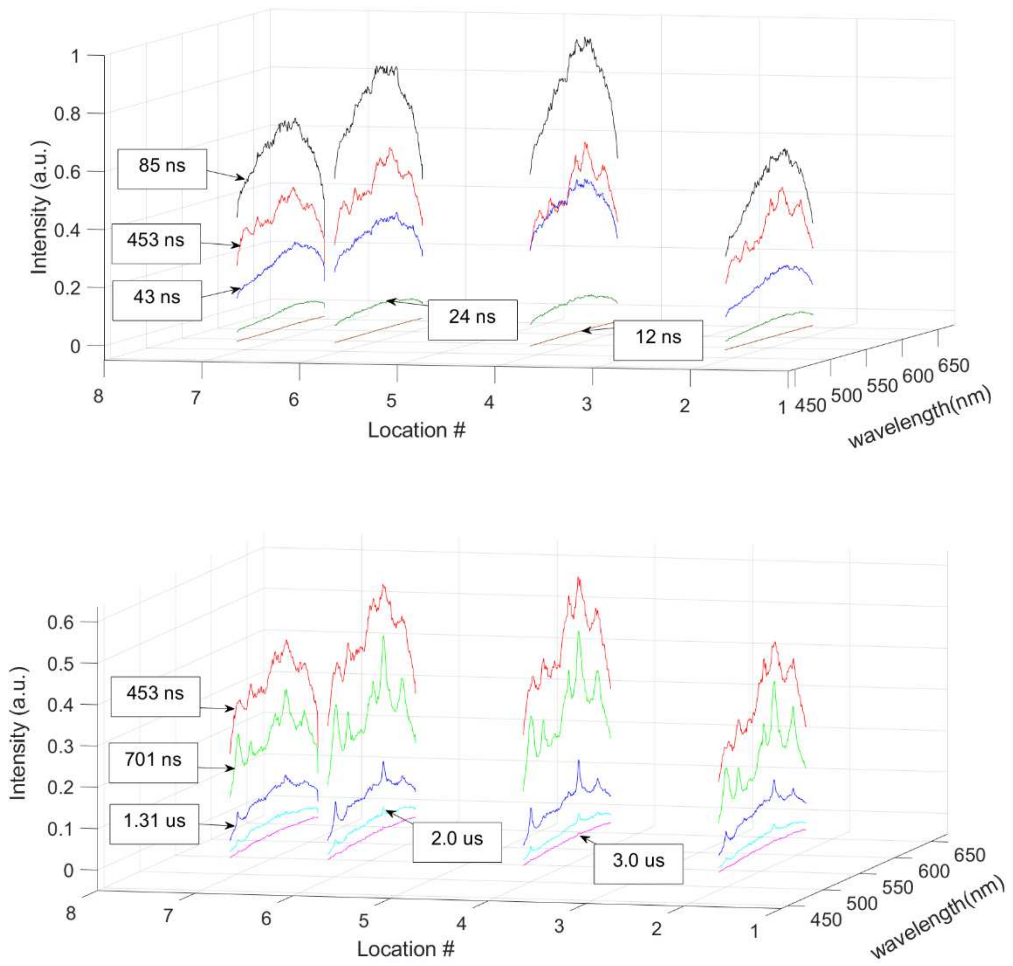
Figure 4-17: Top: 50 kV spatially resolved survey spectra on the rising edge of plasma luminosity. Bottom: same as top but for later times. Time scales of the first observable emission lines increased to ~500 ns after switch closure, consistently later than previous lower voltage test cases
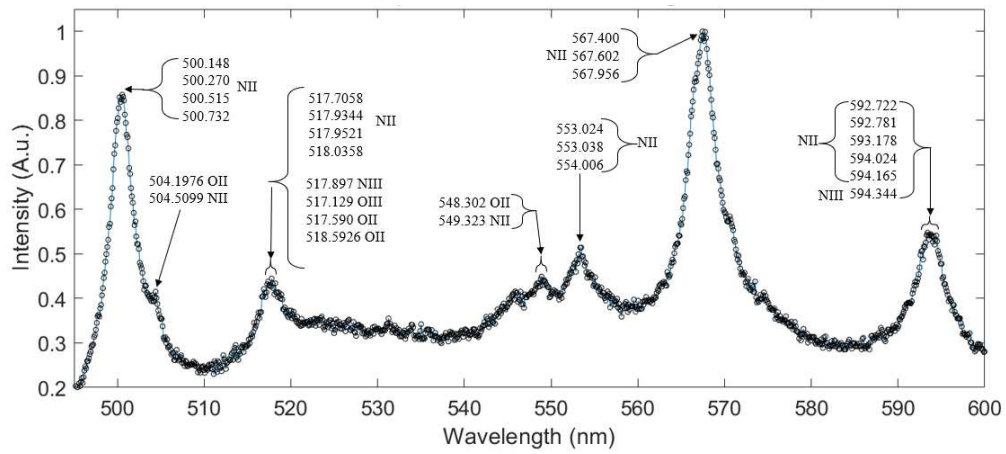
Figure 4-18: Potential constitutive contributing species for switch closure plasma spectra. Data is taken from the 30 kV (1-D) spectra and averaged over all locations at ~800 ns after switch closure

5. <u>Conclusions and Future Work</u>

In conjunction with Sandia National Laboratories (SNL) we have designed and built a new pulsed power test bed at Colorado State University (CSU), the Pulsed Power and Plasma Science Center (P3SC). With growing national and international demand for an environmentally responsible and reliable energy source, SNL's pulsed power program is on the leading edge of controlled fusion research; an exciting and favorable candidate for modern energy generation. Supporting design and development of future pulsed power technology, High Voltage Laser Triggered Switches (HV-LTS) are an integral component to modern Z-pinch style fusion research testbeds. Given this, the current thrust of the P3SC laboratory, and this thesis, is to investigate switch closure plasma characteristics associated with recently discovered gaps in the Tom Martin Switch model which describes the temporal plasma channel resistance of HV-LTSs. Standard electrical characteristics were measured, and switch performance was determined for 2 laser locations, 3 set voltages, 3 percentages of self-break, and 2 fill gasses. Every possible permutation was not tested, instead the differences in laser location, electrical polarization, and fill gas were determined to be paramount, and the final experimental matrix was created with this in mind. Optimum laser location was determined to be on the surface of the cathode with overall laser energy, switch run time, and jitter being consistently lower than with the laser focused to within the gas of the central section between the electrodes. Moreover, for these locations, we find jitter on the order of 100 ps with laser energies below 1 mJ driving switch closure (laser on surface). 10-90 rise times were measured for all test cases and minor differences were observed depending on electrical polarization. Further investigation is necessary to make quantitative determinations, but minimal polarization insensitivity was observed with the laser focused in the center (fill gas).

Overall switch performance was evaluated with a weighted average score based on switch run time, jitter, and percentage of self-break as inputs. Three sets of weightings were using

45

yielding different maps of design space depending on user specified importance. Overall, standard electrical polarization (laser strikes cathode) was determined to yield higher switch performance when prioritizing run time or jitter, but when accounting for run time, jitter, and percentage of self-break, the gap narrowed somewhat. An alternative fill gas (SF_6) was also tested with limited success. The HV-LTS failed to fire reliably with the laser centered in the fill gas, and only at elevated laser energies was command fire accomplished with the laser on the surface. Equivalent circuit resistance and inductance was measured by probing the signal from a CVR and found to be 136 ± 1 nH and 0.21 ± 0.01 Ω respectively (consistent with unpublished work from Josh Leckbee, SNL).

Preliminary switch closure plasma characteristics are presented investigating two core assumptions of the Tom Martin switch model utilizing optical imaging and optical emission spectroscopy (OES) analysis. Schlieren images of the blast wave associated with the laser induced plasma, without the application of an external high voltage, show good agreement with published literature regarding shock wave propagation and third lobe generation. Furthermore, images of switch closure for 50 and 100 kV shots were presented and radial plasma channel growth was extracted. Informing the plasma channel radial growth assumption in the Martin model, this data was fit with an At^k trendline with good agreement and compared to published literature, confirming the radial growth assumption laid out in the Martin model. Ultimately, the exponential factor k, being the primary contributing factor, was found to have an extent of ~ 0.575 - 0.737 and this range of values was found to have an overall impact on the calculation of plasma resistance on the order of 15%. Preliminary OES data are presented of an optically accessible HV-LTS and represent a first publication to the best knowledge of the authors. Additional research may serve to inform the constant conductivity proposed by Martin, in particular one should compute the Spitzer conductivity from temperature. Emission spectra were observed to be dominated by continuum at early times with lines becoming visible ~200 ns after a 30 kV shot and ~500 ns after a 50 kV shot (short circuit configuration). Potential constitutive spectral components

of this plasma have been identified for later times (~800 ns) for a 30 kV shot and appear to be dominated by singly ionized nitrogen species.

Future work may consist of further investigation of HV-LTS plasma spectra to determine electron number density and temperature via OES or other non-contact measurements. Given the strong continuum observed at early times, a more robust optical measurement is necessary in this time regime with Thomson scattering being an attractive alternative. At low number densities the limiting factor for Thomson scattering is typically a low number of scattered photons relative to elastic and Rayleigh scattering signals. We believe that low signal limitations for HV-LTSs are less likely, and high densities may be the main limiting factor. At sufficiently high electron number densities the main limitation of this technique arises when the plasma frequency exceeds the optical frequency of the probe beam such that light can't penetrate the switch closure plasma (plasma mirror). From preliminary calculations, an idealized Thomson measurement at 532 nm would then have an effective upper limit on the order of $4x10^{21}$ cm^{-3} based on this limitation.

Bibliography

[1]   Smith, I., "The early history of western pulsed power," *IEEE Transactions on Plasma Science*, vol. 34, 2006, pp. 1585–1609.

[2]   Arsdall, A. Van, *Pulsed Power at Sandia National Laboratories the first fourty years*, 2007.

[3]   Lindl, J. D., Amendt, P., Berger, R. L., Glendinning, S. G., Glenzer, S. H., Haan, S. W., Kauffman, R. L., Landen, O. L., and Suter, L. J., "The physics basis for ignition using indirect-drive targets on the National Ignition Facility," *Physics of Plasmas*, vol. 11, 2004, pp. 339–491.

[4]   Pendleton, W. K., and Guenther, A. H., "Investigation of a laser triggered spark gap," *Review of Scientific Instruments*, vol. 36, 1965, pp. 1546–1550.

[5]   Udo, T., "Switching Surge and Impulse Sparkover Characteristics of Large Gap Spacings and Long Insulator Strings," *IEEE Transactions on Power Apparatus and Systems*, vol. 84, 1965, pp. 304–309.

[6]   Cravey, W. R., Freytag, E. K., Goerz, D. A., Poulsen, P., and Pincosy, P. A., "Picosecond High Pressure Gas Switch Experiment," *Ninth IEEE International Pulsed Power Conference*, 1993, pp. 483–486.

[7]   Woodworth, J. R., Frost, C. A., and Green, T. A., "uv laser triggering of high-voltage gas switches," *Journal of Applied Physics*, vol. 53, 1982, pp. 4734–4739.

[8]   Guenther, A. H., and Bettist, J. R., "The laser triggering of high-voltage switches," *Journal of Physics D: Applied Physics*, vol. 11, 1978, pp. 1577–1613.

[9]   Beverly, R, E., "Reliable Fiber-Optic Triggering of a 50-kV Switch Using 532-nm Laser Light," *IEEE Transactions on Plasma Science*, vol. 42, 2014, pp. 2962–2967.

[10] Martin, T. H., "Pulse Charged Gas Breakdown," *Fifth IEEE Pulsed Power Conference*, 1985, pp. 74–83.

[11] Peterkin, F. E., and Williams, P. F., "Physical mechanism of triggering in trigatron spark gaps," *Applied Physics Letters*, vol. 53, 1988, pp. 182–184.

[12] Martin, T. H., Seamen, J. F., and Jobe, D. O., "Energy losses in switches," *Ninth IEEE International Pulsed Power Conference*, 1993, pp. 463–470.

[13] Lavrinovich, I. V., and Oreshkin, V. I., "Numerical simulation and analysis of energy loss in a nanosecond spark gap switch," *Journal of Physics: Conference Series*, 2014.

[14] Pouncey, J. C., and Lehr, J. M., "A spark gap model for LTspice and similar circuit simulation software," *Digest of Technical Papers-IEEE International Pulsed Power Conference*, 2015.

15 Struve, K. W., Bennett, L. F., Chavez, T. F., Davis, J. P., Harjes, H. C., Pasik, M., Savage, M. E., Smith, D. L., Stygar, W. A., and Wagoner, T. C., "Circuit-code modeling of the refurbished z accelerator: Comparison of measurements with predictions," *Proceedings of the 2008 IEEE International Power Modulators and High Voltage Conference, PMHVC*, 2008, pp. 94–97.

16 Simpson, S., Johns, O., Rose, C., Luckbee, J., Dumitrache, C., Nielsen, D., Yalin, A., Kiefer, M., "Triggering of a High Pressure Air-filled High Voltage Spark Gap Switch Using Fiber-Delivered Laser Induced Plasmas Resulting in Sub-nanosecond Jitter at Low Percentages of Self-Break," IEEE Pulsed Power Conference, Brighton, United Kingdom June 2017: .

17 Wolford, M. F., Myers, M. C., Hegeler, F., and Sethian, J. D., "Dynamics of Laser Triggered, Gas-Insulated Spark Gaps during Repetitive Operation," *IEEE Transactions on Plasma Science*, vol. 44, 2016, pp. 2410–2423.

18 Kushner, M. J., Kimura, W. D., and Byron, S. R., "Arc resistance of laser-triggered spark gaps," *Journal of Applied Physics*, vol. 58, 1985, pp. 1744–1751.

19 Braginskii, S., "Theory of the Development of a Spark Channel," *J. Exptl. Theoret. Phys. (U.S.S.R.)*, vol. 34, 1958, pp. 1068–1074.

20 Spitzer, Lyman. Harm, R., "Transport Phenomena in Completely Ionized Gas," *Physical Review*, vol. 89, 1953, pp. 977–981.

21 Zeng, Q., Guo, L., Li, X., He, C., Shen, M., Li, K., Duan, J., Zeng, X., and Lu, Y., "Laser-induced breakdown spectroscopy using laser pulses delivered by optical fibers for analyzing Mn and Ti elements in pig iron," *Journal of Analytical Atomic Spectrometry*, vol. 30, 2015, pp. 403–409.

22 El-Rabii, H., Victorov, S. B., and Yalin, A. P., "Properties of an air plasma generated by ultraviolet nanosecond laser pulses," *Journal of Physics D: Applied Physics*, vol. 42, 2009, p. 075203.

23 Thiyagarajan, M., and Thompson, S., "Optical breakdown threshold investigation of 1064 nm laser induced air plasmas," *Journal of Applied Physics*, vol. 111, 2012, p. 073302.

24 Dumitrache, C., Yalin, A., and Shneider, M. N., "Laser Generated Plasma Using a Dual Pulse Approach with Application to Laser Ignition," *45TH AIAA PLASMADYNAMICS AND LASERS CONFERENCE*, 2014, pp. 1–9.

25 Rapp, L., Haberl, B., Bradby, J. E., Gamaly, E. G., Williams, J. S., and Rode, A. V, *Fundamentals of Laser-Assisted Micro- and Nanotechnologies*, 2014.

26 Bradley, D., Sheppard, C. G. W., Suardjaja, I. M., and Woolley, R., "Fundamentals of high-

energy spark ignition with lasers," *Combustion and Flame*, vol. 138, Jul. 2004, pp. 55–77.

27   Vlastos, A, E., "The Resistance of Sparks," *Journal of Applied Physics*, vol. 43, 1972, pp. 1987–1989.

28   Dougal, R. A., and Williams, P. F., "Fundamental processes in the laser-triggered electrical breakdown of gases: Unconventional geometries," *Journal of Applied Physics*, vol. 60, 1986, pp. 4240–4247.

29   Woo, S.-Y., Jeong, D.-H., Seo, K.-B., and Kim, J.-H., " A Study on Dielectric Strength and Insulation Property of SF 6 /N 2 Mixtures for GIS ," *Journal of International Council on Electrical Engineering*, vol. 2, 2012, pp. 104–109.

30   G. Loucas, Christophorou, K. James, Olthoff, S. David, G., "Gases for Electrical Insulation and Arc Interruption: Possible Present and FutureAlternatives to Pure SF6," *National Instutute of Standards and Technology (NIST), Technical Note 1425*, 1997.

31   Dumitrache, C., Wilvert, N., Yalin, A., and Shneider, M., "Laser Plasma Formation Using Dual Pulse Pre-Ionization," *44th AIAA Plasmadynamics and Lasers Conference*, 2013, pp. 1–10.

32   Settles, G, S., *Schlieren and Shadowgraph Techniques: Visualizing Phenomena in Transparent Media*, Springer, 2001.

33   Mazumdar, A., *Principles and Techniques of Schlieren Imaging*, 2013.

34   Martin, T. H., "An empirical formula for gas switch breakdown delay," *Seventh Pulsed Power Conference*, 1989, pp. 73–79.

35   Gebel, G. C., Mosbach, T., Meier, W., and Aigner, M., "Laser-induced blast waves in air and their effect on monodisperse droplet chains of ethanol and kerosene," *Shock Waves*, vol. 25, 2015, pp. 415–429.

36   Sobral, H., Villagrán-Muniz, M., Navarro-González, R., and Raga, A. C., "Temporal evolution of the shock wave and hot core air in laser induced plasma," *Applied Physics Letters*, vol. 77, 2000, pp. 3158–3160.

37   "National Institute of Standards an Technology" Available: physics.nist.gov/cgi-bin/atdata/main asd.

Appendix A

<u>Pressure system calculations and components</u>

Given the designated OP the accumulated pressure is calculated as:

Regulator: Swagelock 0-500 PSIG stainless steel PR regulator $C_v = 0.06$

Bottle: 300 size, zero air, bottle pressure 2250 PSIG, P1=2250+12.2 = 2262 PSIA

Calculated chocked flow as:

$$Q = 0.471 * N_2 * C_v * P1 * \sqrt{\frac{1}{s_g * T_1}} = 62.8 \text{ SCFM}$$

$N_2 = 22.67$, $C_v= 0.06$ (from manufacturer), P1 = 2262 PSIA, $S_g = 1$, $T_1 = 532$

Referencing Swagelock's manual for their PRV6 series PRV the accumulated pressure, defined as the pressure rise above the set pressure should occur if the relief valve had to handle the full regulator flow capacity = Q was determined to be ~ 50 PSI (Figure A-1). The total pressure that the system would see is the PRV pressure + the accumulated pressure or ~ 800 PSI. Given that this switch body was not hydro-statically tested to failure there exists no MAWP. However, FEA calculations by Owen Johns (SNL) show a factor of safety (FOS) of 4 when operating at 500 PSIG, giving an upper limit of ~ 2000 PSIG before failure. Therefore, this equates to a working FOS of ~ 2000/800 = 2.5 for our OP. This FOS was determined to be adequate and the remaining components were specked out to adhere to safe pressure practices. A graphic of the completed pressure components can be seen in the Figure A-2.

PRV6 Series

Flow rates are based on testing of PRV6 series valves with 3/4 in. female ISO/BSP end connections.
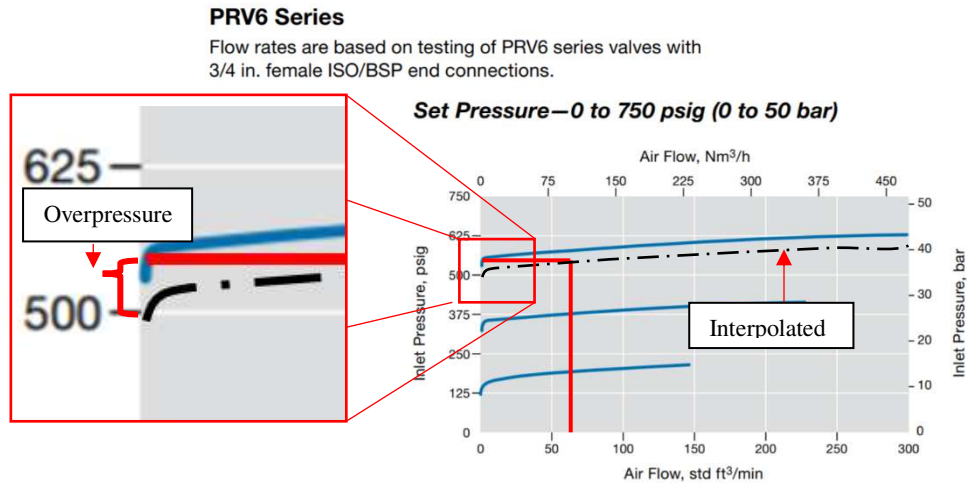
Figure A-1: Credit Swagelok for plot. Overpressure calculation for this given PRV with minimal interpolation found to be ~ 50 PSI
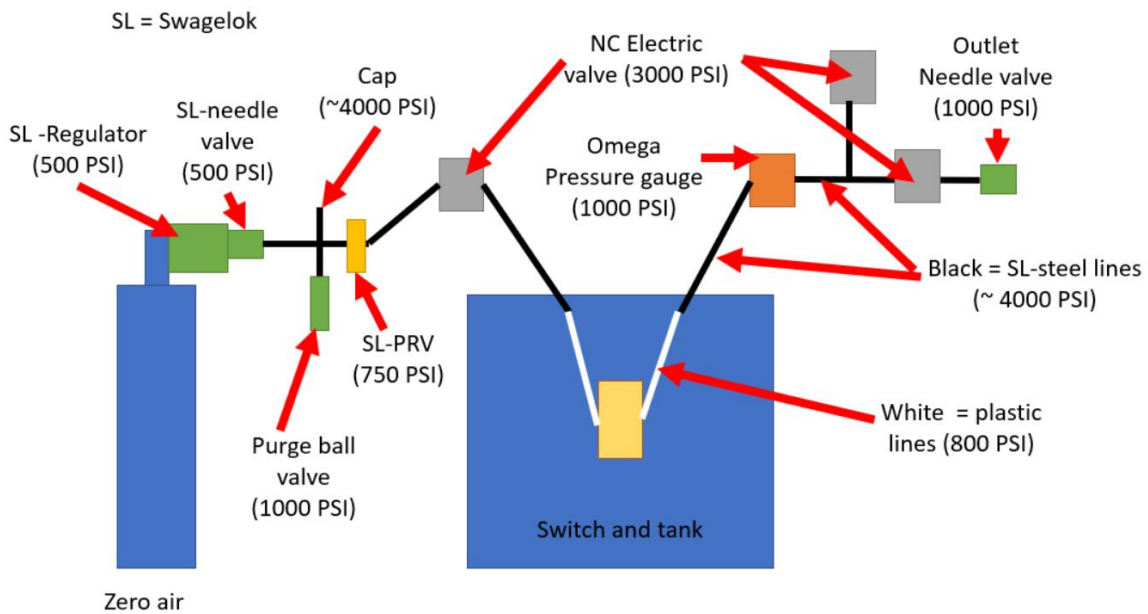
Figure A-2: Pressure components for the 3PSC lab space. Note, the outlet needle valve is used to adjust the outlet flow under specific conditions such that the pressure can be monitored and therefore set remotely with this system.

52

Appendix B

<u>MatLab routine and calculation of resistance and inductance</u>

Data is imported from a user selected folder, and the code searches for XXX.CSV files, with this format being used because it is the native output of Techtronic oscilloscopes. After data is pulled in it is ran through a lowpass filter, zero offset, and the laser rising edge and peak is found (Figure B-1, top left). This peak is defined as then shifted forward in time by the known delay for the time of flight from the laser trigger signal to the laser arriving in the switch (5.5 ns). Following this the 5, 10, and 90 % locations are found along with all subsequent peaks and zero crossings of the current pulse data (Figure B-1, top right). Recall the switch is shot into a short circuit so the resulting waveform is a damped decaying sinusoid. Now with knowledge of all peaks, valleys, zero's and t=0 the code then calculates 10-90 rise time, delay, resistance and inductance. Calculating the inductance of the circuit every other zero location is needed (Figure B-2), I.e. one full cycle using the equation below.

$$L = \frac{\left(\frac{T}{2\pi}\right)^2}{C}$$

Where T is the average period calculated over 8 full cycles (seconds), c is the known capacitance in Farads of the circuit. For this system the circuit capacitance is assumed to be dominated by the two large 20 nf capacitors in parallel giving an equivalent nominal capacitance of 10 nf. From previous literature provided by Josh Leckbee (SNL), these capacitors are not exactly 20 nf and a value of 10.06 nf was measured and was used in all calculations. Moreover, the equations for the inductance and resistance were taken from unpublished work from Josh Leckbee. To calculate the circuit resistance the relative peak amplitudes are used (Figure B-3) along with knowledge of the circuit inductance.

$$R = \frac{2L \ln\left(\frac{I}{I'}\right)}{\Delta t}$$

L is the previously calculated inductance in Henry's, I is the first peak and I' is its closest neighbor

to the right (I/I' is unitless) and Δt is the time difference between these peaks in seconds. Note,

the value of the resistance was averaged over the first 5 cycles, then averaged over 5 shots for

each measurement.
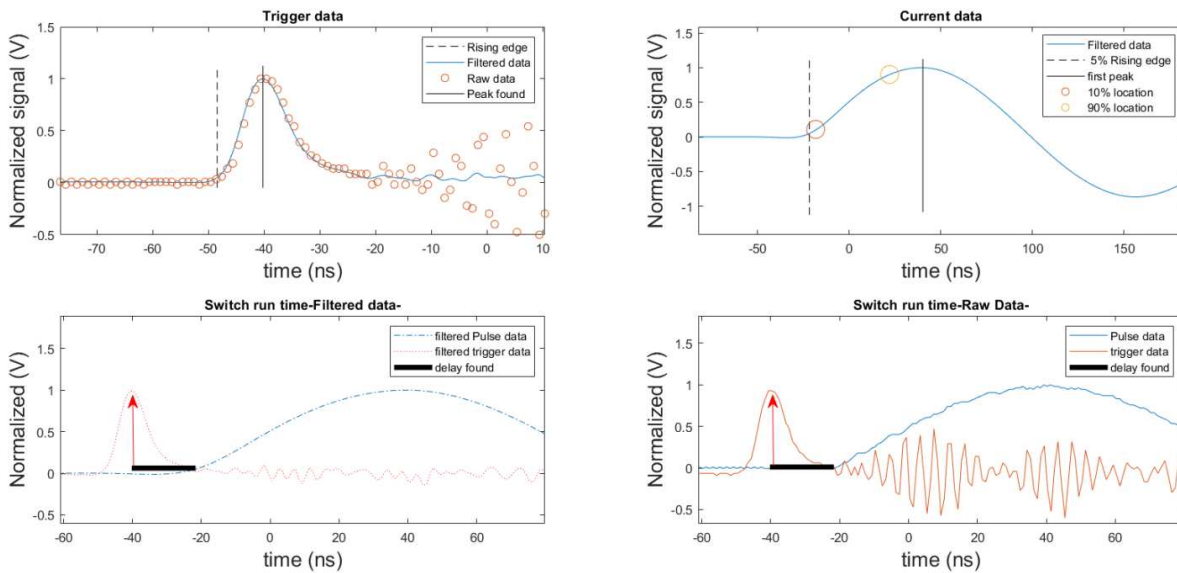
Figure B-1: Top left: rising edge and peak found for trigger data (laser), Top Right: 5, 10, and 90% of first peak of current data found. Bottom Left: filtered data showing switch run time found, Bottom Right, raw data showing switch run time found
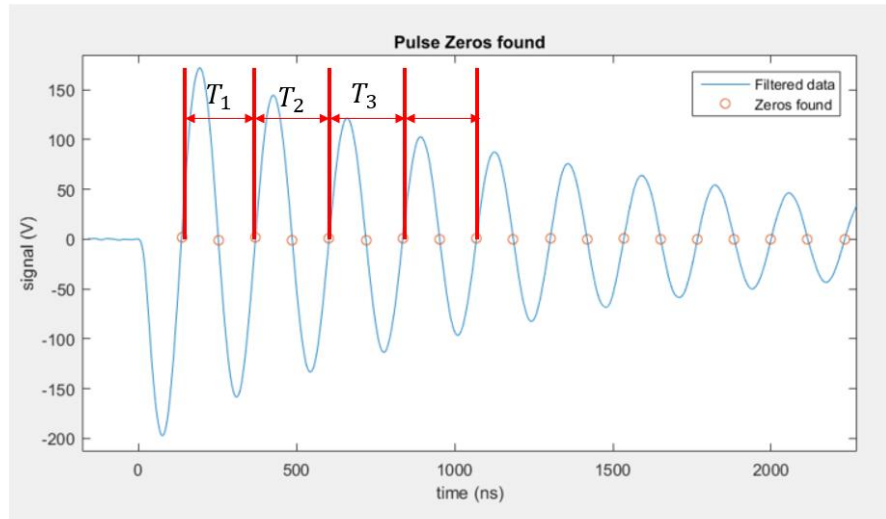
Figure B-2: Calculation of the inductance requires knowledge of the periodicity of the decaying sinusoid.
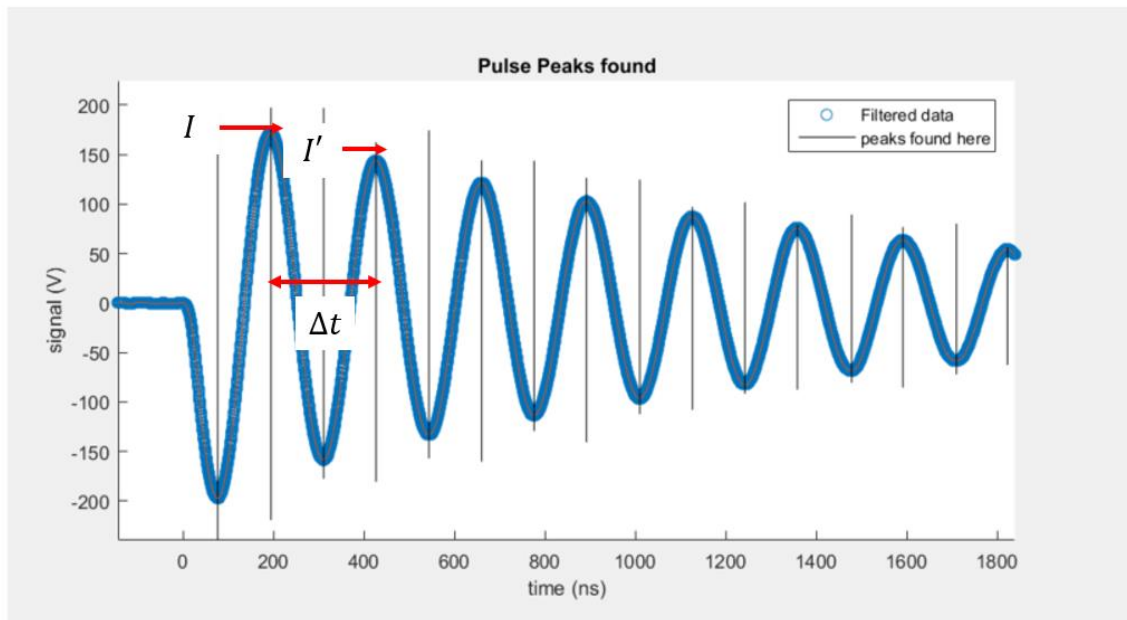
Figure B-3: Calculation of the resistance requires knowledge of the inductance calculated previously. Following this the relative amplitude of the decaying sinusoid can then be used to compute the resistance.